Theses and Dissertations                    1. Thesis and Dissertation Collection, all items

2012-06

# In Situ Raman Spectroscopy of the Nanodiamond-to- Carbon Onion Transformation During Thermal Annealing of Detonation Nanodiamond Powder

Cebik, Jonathan E.

Monterey, California. Naval Postgraduate School

http://hdl.handle.net/10945/7318

# NAVAL
# POSTGRADUATE
# SCHOOL

## MONTEREY, CALIFORNIA

# THESIS

## *IN SITU* RAMAN SPECTROSCOPY STUDY OF THE NANODIAMOND-TO-CARBON ONION TRANSFORMATION DURING THERMAL ANNEALING OF DETONATION NANODIAMOND POWDER

by

Jonathan E. Cebik

June 2012

| | |
|---|---|
| Thesis Advisor: | Sebastian Osswald |
| Second Reader: | Joseph Hooper |

**Approved for Public Release; distribution is unlimited**

THIS PAGE INTENTIONALLY LEFT BLANK

| 1. AGENCY USE ONLY (Leave blank) | 2. REPORT DATE <br> June 2012 | 3. REPORT TYPE AND DATES COVERED <br> Master's Thesis | |
|---|---|---|---|
| **4. TITLE AND SUBTITLE** In Situ Raman Spectroscopy of the Nanodiamond-to-Carbon Onion Transformation During Thermal Annealing of Detonation Nanodiamond Powder | | **5. FUNDING NUMBERS** | |
| **6. AUTHOR(S)** Jonathan E. Cebik | | | |
| **7. PERFORMING ORGANIZATION NAME(S) AND ADDRESS(ES)** <br> Naval Postgraduate School <br> Monterey, CA 93943-5000 | | **8. PERFORMING ORGANIZATION REPORT NUMBER** | |
| **9. SPONSORING /MONITORING AGENCY NAME(S) AND ADDRESS(ES)** <br> N/A | | **10. SPONSORING/MONITORING AGENCY REPORT NUMBER** | |

**11. SUPPLEMENTARY NOTES** The views expressed in this thesis are those of the author and do not reflect the official policy or position of the Department of Defense or the U.S. Government.  IRB Protocol number _____N/A_____.

| 12a. DISTRIBUTION / AVAILABILITY STATEMENT <br> Approved for public release; distribution is unlimited | 12b. DISTRIBUTION CODE <br> A |
|---|---|

**13. ABSTRACT (maximum 200 words)**

In this study, *in situ* Raman spectroscopy is utilized to investigate the onset of nanodiamond (ND) graphitization, the conversion of diamond ($sp^3$) to graphitic ($sp^2$) carbon, and the subsequent formation of carbon onions.  Although the ND-to-carbon onion transformation through thermal annealing of ND in vacuum or inert atmosphere at high temperatures is a well-known phenomenon, the kinetics of the transformation and related structural changes in the nanocrystals are yet not fully understood.  Using a high temperature stage under inert atmosphere, the Ultraviolet (UV) Raman spectra of ND were recorded during thermal annealing under isothermal and non-isothermal conditions to monitor the structural transformation of ND crystals at temperatures ranging from 25 to 1100 °C.  To complement the UV Raman spectroscopy studies, X-ray diffraction, high-resolution transmission electron microscopy, and thermogravimetric analysis were performed on bulk samples of annealed ND powders.

The results obtained in this study demonstrate that the ND-to-carbon onion transformation starts with the surface graphitization of smaller ND crystals at temperatures as low as 600–700 °C.  Between 900–1000 °C, the ND crystals begin to convert to carbon onions from the surface inward. Our study further revealed that the level of surface graphitization and the subsequent transformation of the ND during thermal annealing are strongly dependent on annealing temperature, annealing time, and ND crystal size.  The gained knowledge does not only provide better understanding of the ND-to-carbon onion transformation mechanism and therefore allow for an optimization of the carbon onion synthesis process, but also enables the fabrication of ND with various degrees of surface graphitization. These hybrid ND/carbon onion particles have unique physical and chemical properties that are expected to lead to a completely new set of applications, particularly in energy storage.

| 14. SUBJECT TERMS carbon nanomaterials, nanodiamond, carbon onion, onion-like carbon, carbon nano-onions, onion-like fullerenes, Raman spectroscopy, x-ray diffraction, transmission electron microscope, thermogravimetric analysis | 15. NUMBER OF PAGES <br> 75 |
|---|---|
| | 16. PRICE CODE |

| 17. SECURITY CLASSIFICATION OF REPORT <br> Unclassified | 18. SECURITY CLASSIFICATION OF THIS PAGE <br> Unclassified | 19. SECURITY CLASSIFICATION OF ABSTRACT <br> Unclassified | 20. LIMITATION OF ABSTRACT <br> UU |
|---|---|---|---|

i

THIS PAGE INTENTIONALLY LEFT BLANK

**IN SITU RAMAN SPECTROSCOPY STUDY OF THE NANODIAMOND-TO-CARBON ONION TRANSFORMATION DURING THERMAL ANNEALING OF DETONATION NANODIAMOND POWDER**

Jonathan E. Cebik
Lieutenant, United States Navy
B.S.E., University of Connecticut, 2005

Submitted in partial fulfillment of the
requirements for the degree of

**MASTER OF SCIENCE IN APPLIED PHYSICS**

from the

**NAVAL POSTGRADUATE SCHOOL**
**June 2012**

Author:           Jonathan E. Cebik

Approved by:      Sebastian Osswald
                  Thesis Advisor

                  Joseph Hooper
                  Second Reader

                  Andres Larraza
                  Chair, Department of Physics

THIS PAGE INTENTIONALLY LEFT BLANK

# ABSTRACT

In this study, in situ Raman spectroscopy is utilized to investigate the onset of nanodiamond (ND) graphitization, the conversion of diamond (sp3) to graphitic (sp2) carbon, and the subsequent formation of carbon onions. Although the ND-to-carbon onion transformation through thermal annealing of ND in vacuum or inert atmosphere at high temperatures is a well-known phenomenon, the kinetics of the transformation and related structural changes in the nanocrystals are yet not fully understood. Using a high temperature stage under inert atmosphere, the Ultraviolet (UV) Raman spectra of ND were recorded during thermal annealing under isothermal and non-isothermal conditions to monitor the structural transformation of ND crystals at temperatures ranging from 25 to 1100 °C. To complement the UV Raman spectroscopy studies, X-ray diffraction, high-resolution transmission electron microscopy, and thermogravimetric analysis were performed on bulk samples of annealed ND powders.

The results obtained in this study demonstrate that the ND-to-carbon onion transformation starts with the surface graphitization of smaller ND crystals at temperatures as low as 600–700 °C. Between 900–1000 °C, the ND crystals begin to convert to carbon onions from the surface inward. Our study further revealed that the level of surface graphitization and the subsequent transformation of the ND during thermal annealing are strongly dependent on annealing temperature, annealing time, and ND crystal size. The gained knowledge does not only provide better understanding of the ND-to-carbon onion transformation mechanism and therefore allow for an optimization of the carbon onion synthesis process, but also enables the fabrication of ND with various degrees of surface graphitization. These hybrid ND/carbon onion particles have unique physical and chemical properties that are expected to lead to a completely new set of applications, particularly in energy storage.

THIS PAGE INTENTIONALLY LEFT BLANK

# TABLE OF CONTENTS

# LIST OF FIGURES

# LIST OF ACRONYMS AND ABBREVIATIONS

| | |
|---|---|
| Argon | Ar |
| CNO | Carbon nano-onions |
| HRTEM | High resolution transmission electron microscopy |
| IR | Infrared |
| M@OLF | Metal encapsulating onion-like fullerenes |
| ND | Nanodiamond |
| OLC | Onion-like carbon |
| OLF | Onion-like fullerenes |
| SNR | Signal-to-noise ratio |
| TGA | Thermogravimetric analysis |
| UV | Ultraviolet |
| XRD | X-ray diffraction |

THIS PAGE INTENTIONALLY LEFT BLANK

# ACKNOWLEDGMENTS

THIS PAGE INTENTIONALLY LEFT BLANK

# I. INTRODUCTION

## A. CARBON ONIONS

### 1. Carbon Onion Structure and Synthesis

Carbon onions, also known as onion-like carbon (OLC), onion-like fullerenes (OLFs), or carbon nano-onions (CNOs) [1], are a unique class of nanomaterial, often referred to as the zero-dimensional pendant to multi-wall carbon nanotubes. Recent improvements in synthesis techniques and a rapidly increasing number of potential applications have sparked growing interest in these unique nanostructures during recent years. Current applications include, but are not limited to, solid lubrication [2], composites [3], electromagnetic shielding [4], high-conductivity materials and superconductors [5], gas storage [6], photovoltaics and fuel cells [7], special performance catalyst [8] and energy storage [9–12].

Carbon onions are a member of the fullerene family and can be imagined as quasispherical, closed-shell nanostructures consisting of several concentric, fullerene-like spheres of different diameters, stacked into each other (typically between 3 and 8) [13, 14]. Outer diameters range from 5 up to 100 nm and the inner core are either hollow or filled with a different phase of carbon (e.g., diamond) or metal catalyst, sometimes referred to as metal-encapsulating onion-like fullerenes (M@OLFs) [9]. Figure 1 shows a schematic of the atomic structure of a typical carbon onion.
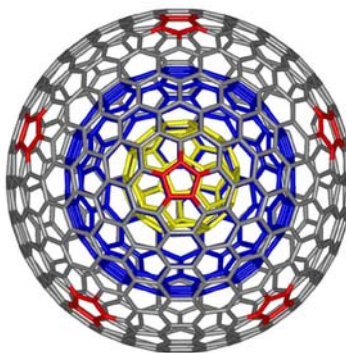
Figure 1.    Atomic structure of a carbon onion consisting of three hexagonal layers. The grey shell is the outermost layer while the second and third are blue and yellow respectively.  The red polygons in the outer layer denote the pentagons, which are required to obtain a curvature in the hexagonal sheet (From [14]).

Carbon onions have been produced by numerous means, including arc discharge [15], electron-beam irradiation [16], chemical vapor deposition [17–19], RF plasma [20], carbon ion-implantation [21], thermolysis [22], solid-state carbonization [23], and thermal annealing of nanodiamond [24, 25].  While the majority of carbon onion research has been devoted to identifying suitable synthesis and purification methods, most of the existing production methods still suffer from either small synthesis volumes and limited scalability, insufficient process control, excessive co-synthesis of byproducts (impurities), or require complex and expensive processing equipment.  However, a proper investigation of the physical and chemical properties of carbon onions requires macroscopic quantities with well-defined properties.  At present, the most effective method for carbon onion production is thermal annealing of nanodiamond (ND) powder.

## 2.    Nanodiamond Structure and Synthesis

Diamond, an allotrope of carbon, is among the hardest materials known to date, and has extremely desirable physical and chemical properties.  Diamond consists of $sp^3$-bonded carbon atoms that are arranged to a tetrahedral, FCC-type lattice structure. Nanodiamond (ND) powders consist of nanometer-sized diamond crystals that possess the favorable properties and structure of diamond, but provide additional advantages due to their confined size.  In contrast to bulk diamond, the ND average crystal size is around

2

5 nm.  Currently, two main methods for the fabrication of ND are utilized: the transformation of graphite under high temperature and pressure and detonation of carbon-based explosive materials (detonation ND) [13].  Most commonly, detonation ND is produced from the detonation of trinitrotoluene (TNT) and cyclotrimethylenetrinitramine (RDX) in an oxygen-deficient hermetic tank [24].  The products of the detonation are diverse and must then be treated to obtain pure ND.

Detonation ND is used most frequently in ND-to-carbon onion studies since it is commercially available.  In most commercial ND used for thermal annealing, the ND precursor has already been purified from amorphous carbon and catalyst impurities and since the thermal annealing process does not require any additional catalyst, the purity of the carbon onions sample remains high.  Furthermore, the size distribution and structural variety of the carbon onions is relatively narrow as compared to other synthesis methods, and can be controlled by adjusting the size distribution of the ND powder prior to the annealing process.

### 3.      Annealing Nanodiamond

In 1992 Ugarte observed that carbon soot was transformed into quasi-spherical particles with concentric graphitic shells under intense radiation from an electron beam and described these particles as 'onions' [1].  Later Deheer and Ugarte heat treated carbon soot at temperatures up to 2400 °C creating carbon onions and other carbon nanoparticles, while analyzing them from high resolution transmission electron microscopy (HRTEM) micrographs and their visible and ultraviolet absorption spectra.  Their similarity to the 217.5 nm interstellar absorption feature was also discussed [26].  Kuznetsov et al. first reported details of the formation of OLC through the annealing in vacuum of ultra-disperse diamond (nanodiamond) at temperatures between 1000 and 1500 °C in 1994.  With HRTEM analysis they observed in the annealing products quasi-spherical, polyhedron, and elongated OLC particles.  They noted that the structural transformation begins on the surface of the nanodiamond and progresses inward to the bulk crystal [24].  Figure 2 shows a rudimentary diagram of the annealing transformation of ND to carbon onion.
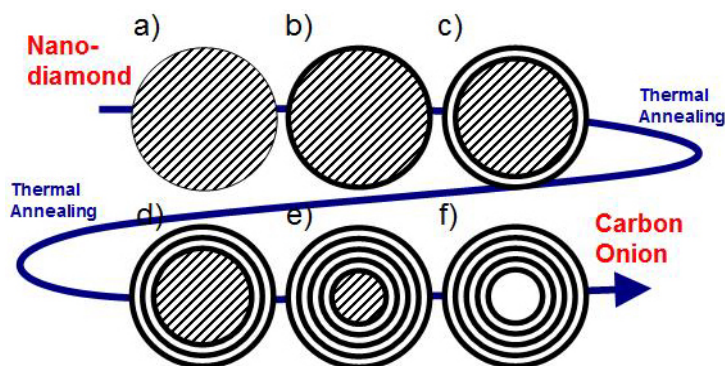
Figure 2.    Basic representation of the structural changes during thermal annealing of ND.  Note that the initial ND size determines the final size of the carbon onions.

In 1998, Obraztsova et al. annealed 5 nm nanodiamond particles at 1100, 1400, 1800, and 2100 K for 1 hour and performed Raman and HRTEM identification of the annealing products.  They observed the first traces of carbon onion formation at 1400 K (1127 °C) and almost full transformation at 1800 K (1527 °C) observing particles with six to seven onion shells.  At higher annealing temperatures (1827 °C) they detected that the carbon onion reconfigured into a highly ordered hexagonal three-dimensional graphite structure [27].  Chen and co-workers thermally annealed ND powder for 1 hour in an argon atmosphere at ambient pressure and temperatures ranging from 300 up to 1150 °C.  Their study revealed a partial ND-to-carbon onion transformation at elevated temperatures (>900 °C), but no data on carbon onion content, size, and shape was presented [28].  Similarly, Qiao et al. synthesized carbon onions by annealing ND powder for 1 hour at temperatures between 1100 and 1400 °C in an argon atmosphere. They reported that onion-like carbons begin to form at temperatures around 1100–1200 °C and transformation temperature changes with the original nanodiamond particle size.  A 4-step model that described the annealing process and the ND-to-onion transformation was presented which included formation of graphite fragments, connection and curvature of graphitic sheets between diamond {111} planes, and closure of graphite layers [29].

Figure 3 is a schematic of their proposed 4-step model. The molecular dynamic simulations and thermodynamic consideration by Leyssale et al. [30] and Kwon et al. [31], respectively, support these results.
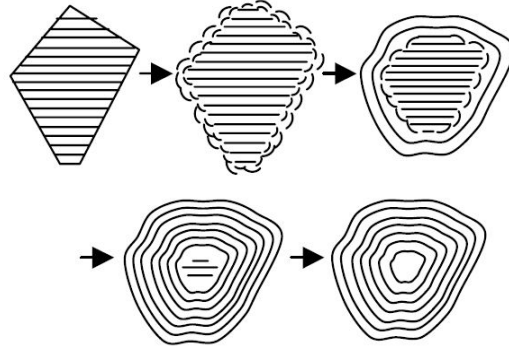


Figure 3.    4-Step model of the ND-to-carbon onion transformation as presented by Qiao et al.  (From [29]).

Butenko et al. studied the surface chemistry of detonation ND and observed the onset of ND graphitization at a temperature of 950 °C through X-ray photoelectron spectroscopy [32]. Bulusheva et al. annealed ND at 1170, 1600, 1900, and 2140 K and utilized x-ray emission spectroscopy to examine the structure of the created carbon onion and graphite/diamond composites [33] and later analyzed quasispherical and polyhedral carbon onions created through vacuum annealing using X-ray absorption spectroscopy [25]. Osipov et al. examined the time evolution of the nanodiamond to graphite and carbon onion process by annealing at 1600 °C for various time intervals. Their analysis through HRTEM and XRD demonstrated that spherical carbon onions were created after annealing for short intervals, while longer annealing times produced polyhedral shaped structures [34]. In 2009 and 2010, Zou and co-workers presented detailed studies on the graphitization of ND at temperatures ranging from 500 to 1400 °C [35–39]. Using HRTEM and Raman spectroscopy they concluded that, during vacuum annealing (1.5 hours at 1Pa) at temperatures around 600 °C (for 1.5 hours), the edge of ND particles started to transform into amorphous carbon, resulting in a complete amorphization of the ND crystals at ~750 °C, followed by onion formation along the edge sites at 850 °C . At the annealing temperature of ~1000–1100 °C, carbon onions with sizes of 5 nm and

5

below were fully converted, while fabrication of carbon onions with larger diameters (> 5 nm) occurred only at temperatures above 1200 °C.  Xie et al. annealed nanodiamond at 900 and 1500 °C in nitrogen ambient and using x-ray photoelectron spectroscopy (XPS) and Raman spectroscopy concluded that annealing at 900 °C does not produce detectable graphitization, but only causes the thermal decomposition of surface groups,  while annealing at 1500 °C formed onion-like carbon with a small diamond core [40].  More recently Petit et al. studied the graphitization of annealed ND also using XPS.  In contrast to Xie's conclusions, they observed that below 900 °C the ND surface is reconstructed into graphite, but the diamond core is unaltered.  Subsequently, above 900 °C $sp^3$ is changed to $sp^2$ from the surface inward toward the diamond core.  They concluded that annealing under vacuum at lower temperatures is an effective method to separate surface and bulk graphitization of the nanodiamond [41].

The benefit of UV Raman spectroscopy to analyze annealed ND was demonstrated by Mykhaylyk and others.  They recognized that UV Raman spectroscopy can effectively detect the initial stages of the graphitization of the ND exterior surface where mixed $sp^2/sp^3$ bonds are reconstructed into simple $sp^2$ bonds [42].  UV laser excitation is particular suitable for ND characterization due to fulfillment of the resonance condition as will soon be discussed.

## B.    RAMAN EFFECT

On 28 February, 1928 Chandrasekhara Venkata Raman performed an experiment which revealed the inelastic scattering of light [43].  This phenomenon is known as the Raman Effect or Raman scattering.  This discovery earned him the Nobel Prize in Physics 1930 "for his work on the scattering of light and the discovery of the effect named after him" [44].

The Raman Effect can be explained both through the classical picture of light scattering and a quantum mechanical model.  First, the classical picture will be discussed.  The classical picture of light scattering deals with a molecular system and an incident oscillating electromagnetic field (light).  The primary field upsets the charge distribution and creates a dipole moment in the system.  Nearby induced dipole moments act together

and their sum creates a secondary electric field irradiated by the molecules, which represents the scattered light [45]. The induced dipole, μ, is given by:

$$\mu = \alpha E,$$
(1)

where $E$ is the external electric field, with amplitude $E_0$ and frequency $\omega_0$, and $\alpha$ is the molecular polarizability of the material. The real part of the field is expressed as:

$$E = E_0 \cos(\omega_0 t).$$
(2)

The molecular polarizability represents how much the electric field is able to disturb the electron density of the sample out of its normal configuration. This value is not constant and can be Taylor expanded around the system's equilibrium nuclear geometry $Q_0$, with $Q$ representing the group of all individual modes $q$:

$$\alpha = \alpha(Q) = \alpha_0 + \sum_{q=1}^{N} \left[ \left( \frac{\partial \alpha}{\partial q} \right)_{q_0} \cdot q + \frac{1}{2} \left( \frac{\partial^2 \alpha}{\partial q \partial q'} \right)_{q_0 q_0'} \cdot q \cdot q' + O\left( q^3 \right) \right].$$
(3)

Each normal coordinate $q$ can be excited with characteristic frequency $\omega_q$, therefore we can write:

$$q = q_0 \cdot \cos(\omega_q t).$$
(4)

Truncating the Taylor expansion in (3) to the linear term (electrical harmonic approximation), and inserting (2), (3), and (4) into (1) produces

$$\mu(t) = \left[ \alpha_0 + \left( \frac{\partial \alpha}{\partial q} \right)_{q_0} \cdot q_0 \cdot \cos(\omega_q t) \right] \cdot E_0 \cdot \cos(\omega_0 t).$$
(5)

Expanding (1.5) by using the product of two cosine functions trigonometric formula we finally obtain

$$\mu(t) = \alpha_0 \cdot E_0 \cdot \cos(\omega_0 t) + \frac{1}{2} \left( \frac{\partial \alpha}{\partial q} \right)_{q_0} \cdot q_0 \cdot E_0 \cdot \cos[(\omega_0 - \omega_q)t]$$
$$+ \frac{1}{2} \left( \frac{\partial \alpha}{\partial q} \right)_{q_0} \cdot q_0 \cdot E_0 \cdot \cos[(\omega_0 + \omega_q)t]$$
(6)

The resulting expression of the time induced dipole moment has three separate, distinct frequency terms that can be used to describe the possible outcomes of light interaction with matter. The first term, $\alpha_0 \cdot E_0 \cdot \cos(\omega_0 t)$, produces scattered light at

frequency $\omega_0$ which is the identical frequency of the incident light. This scattered light has the same energy and is the elastic, or Rayleigh scattering. The next two terms represent inelastic scattering and have different frequencies than the incident light and are referred to as Raman scattering, or the Raman Effect. The second term creates scattered light with frequency $\omega_0 - \omega_q$. With lower frequency and thus lower energy, this is the termed as Raman Stokes scattering. Through $\omega_q$ this term contains information about the molecular system and thus becomes one of the fundamental bases of Raman spectroscopy. The third term in Equation (6) provides for one more scattering possibility, that is, light with frequency higher than the incident light. The emitted light with frequency $\omega_0 + \omega_q$ is termed the anti-Stokes scattering. The spectrum of the anti-Stokes scattering is identical to the Stokes spectrum but has a greatly reduced intensity.

Figure 4 shows a schematic detailing the Raman Effect. First, in (a) the incident light causes an oscillation in the molecular dipole moment at the incident light frequency $v_0$. Next, in (b), the molecule's polarizability changes which causes a variation in the amplitude of the dipole moment oscillation. The result is an oscillation with frequency $v_0 \pm v_m$. Here $v_0 = \dfrac{\omega_0}{2\pi}$ and $v_m = \dfrac{\omega_q}{2\pi}$. The three possible resultant cases that can emit light are shown in (d).
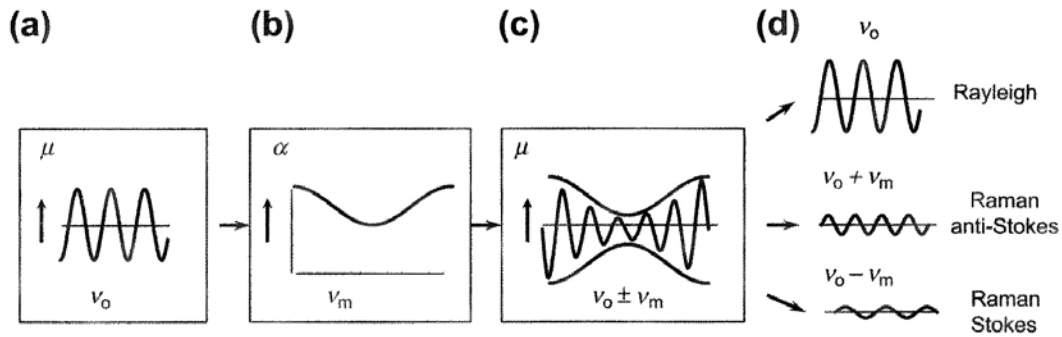


Figure 4.    Rayleigh and Raman scattering in the classical picture of light scattering
(From [46])
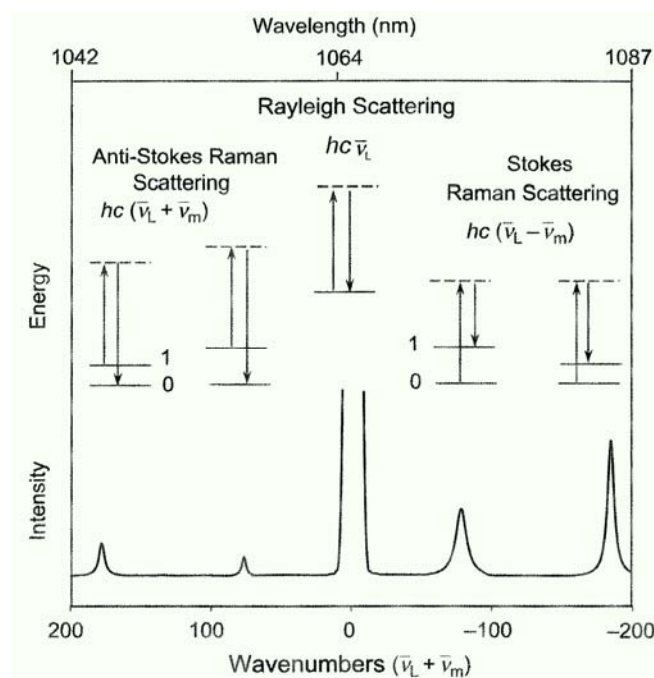
Figure 5.  Rayleigh and Raman scattering (From [46]).

However, the classical picture of light scattering and the Raman Effect does have some shortfalls.  For instance, the classical wave theory description does not assign discrete frequencies to rotational transitions.  Additionally, the Raman scattering tensor is not associated with transitional dipole moments, the molecular Hamiltonian, and the frequency of incident fields.  Consequently, important application of the Raman Effect such as resonance Raman scattering cannot be explained by the classical theory [45].  Therefore, a quantum mechanical approach to light-matter interactions must be considered.

The Raman Effect can also be discussed in terms of the quantum mechanical perturbation theory in which the Rayleigh and Raman scattering are two photon processes involving the scattering of incident light from a "virtual state" [46].  A photon is absorbed by a transition from the ground to virtual state and a new photon is emitted by a departure from this virtual state.  The emitted photon is most probable to have the same frequency as the incident light and therefore be Rayleigh scattered.  In this case, the photon is elastically scattered and results from the transition from the virtual state back to the

ground state, and therefore will have the same energy and frequency as the incident light. Rayleigh scattered intensity is about $10^{-3}$ times less than the incident intensity [46].

Raman scattering occurs with much less probability than Rayleigh scattering having intensity on the order of $10^6$-times less intensity than the incident light [46]. The transition from the virtual state to the first excited state of the vibration causes a Raman scattered photon. The molecule ends up with a different molecular vibrational energy $(\bar{V}_m)$ and scattered photon has different energy and frequency and thus is considered an inelastic process. Figure 5 shows the two possibilities of Raman scattering, Stokes and anti-Stokes. The type of scattering that occurs is dependent on the initial vibrational state of the molecule. A molecule initially in the ground state yields Stokes scattering and one in a vibrational excited state produces anti-Stokes Raman scattering. The relative intensities of the Stokes and anti-stokes Raman signals are governed by the absolute temperature of the sample and energy differences of the ground and excited states. At ambient temperature most molecules are in the ground state, thus the Raman Stokes radiation is much more intense than the Raman anti-Stoke Radiation.

## C.    RAMAN SPECTROSCOPY

### 1.    Raman Signal Intensity

Equation (7) describes the intensity of the Raman scattered radiation $I_R$. Here, as utilized in Raman spectroscopy, the incident light, or excitation source, is a monochromatic laser light. $I_O$ is the incident laser intensity, $v$ is the laser frequency, $N$ is the number of scattering molecules in a given state, $\alpha$ is the polarizability of the molecules, and $Q$ is the vibrational amplitude.

$$I_R \propto v^4 I_O N \left( \frac{\partial \alpha}{\partial Q} \right)^2 \tag{7}$$

In Raman spectroscopy, the Raman scattered radiation $I_R$, is detected by a sensor. Therefore Equation (7) reveals several important parameters of the detected Raman signal. First, the intensity is concentration dependent, so a larger sample will increase the

signal.  Second, increasing the frequency (decreasing wavelength) or power of the excitation laser will increase the signal as well.  However, these effects are more complicated, as the laser excitation wavelength can be matched to the sample material to enhance resonance effects and increasing incident laser power can cause undesired effects such as thermal heating as we shall soon discuss.  Lastly it is important to note that only molecular vibrations which cause a change in the molecular polarizability of the sample are Raman active (i.e. produce Raman scattering).  Specifically, the change in polarizability with respect to the change in vibrational amplitude must be non-zero.

$$\left(\frac{\partial \alpha}{\partial Q}\right) \neq 0 \tag{8}$$

## 2.      Dispersive Raman Spectrometer Light Path
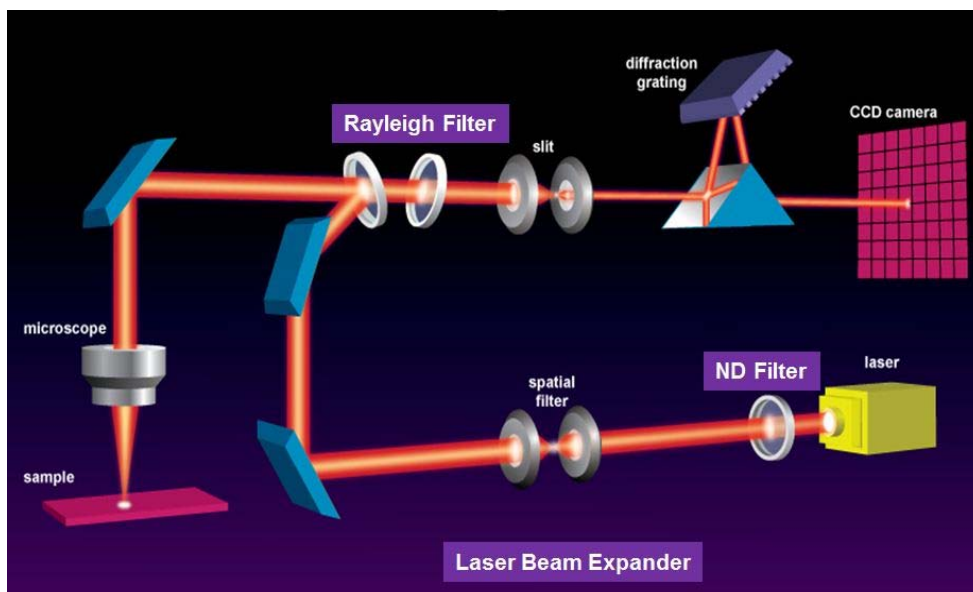


Figure 6.     Light path within a dispersive Raman spectrometer (Renishaw)

Figure 6 shows the path of the excitation source (laser light) and the path of the collective Rayleigh and Raman scattered light after interaction with the sample.  First, the laser light passes through neutral density and spatial filters and then is reflected through the microscope objective onto the sample.  Simultaneous with the excitation laser light

11

being projected onto the sample, Rayleigh and Raman scattered light is emitted from the Raman active material back through the objective. The scattered light then travels a new path through a Rayleigh filter where all light with wavelength identical to the excitation source is rejected. Next, to create a Raman spectrum containing useful information on the molecular structure of the sample, the collected Raman scattered light must be separated into its composite wavelengths. In dispersive Raman instruments the Raman scattered light is focused onto a diffraction grating which splits the light beam into its constituent wavelengths. This light is focused onto a silicon charge-couple device (CCD) detector. From the intensity and wavelength data collected by the CCD, the device software then creates and displays a Raman spectrum. The spectrum is displayed in an x-y plot traditionally with intensity (counts) on the y-axis and wavenumber (wavelength) on the x-axis. Units of cm$^{-1}$are most commonly used for wavenumber. The resultant spectra of peaks and valleys can then be analyzed so that meaningful data about the sample can be extracted.

Figures 7 and 8 display a Renishaw inVia Raman spectrometer. Figure 7 shows the entire spectrometer and microscope system, while Figure 8 details the interior optics. Similar to Figure 6, the light path has been highlighted. The lenses A, B, C, and diffraction grating are changed depending on the excitation source wavelength.



Figure 7.    Renishaw inVia Raman Spectrometer
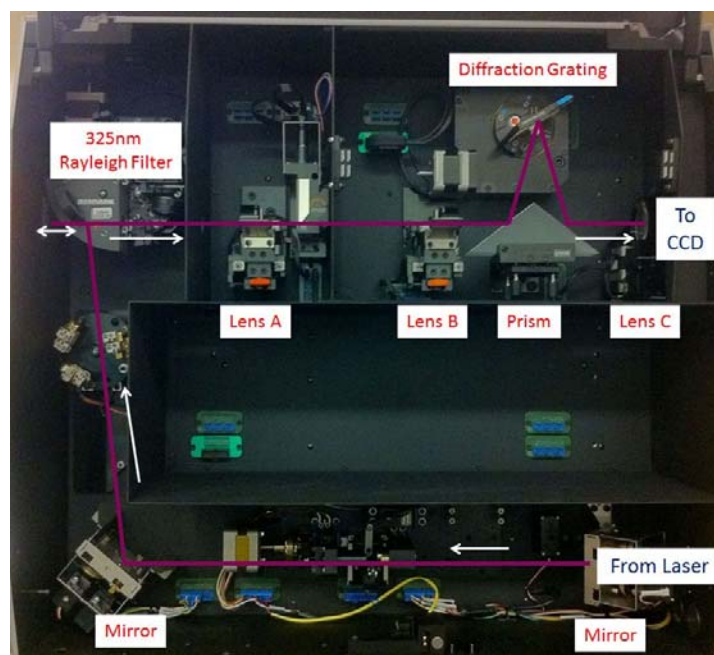
Figure 8.    Renishaw inVia Raman Spectrometer Internals

## 3.    Advantages and Uses of Raman Spectroscopy

Raman spectroscopy is a widely used characterization tool and its advantages over other characterization techniques are vast.  Raman spectroscopy is non-destructive, requires little or no sample preparation, each measurement is fast and inexpensive, qualitative and quantitative analysis is possible, any phase can be measured, small areas down to 1 um can be measured, and samples can be measured through containment windows such as glass or sapphire.

Uses for Raman spectroscopy are expansive.  Characteristic Raman frequencies can be used to determine material composition.  Changes in the frequency of the Raman peak can identify a materials stress/strain state.  Polarization of a Raman peak can reveal crystal symmetry and orientation.  Width of Raman peaks provide information of the quality of the crystal as will be discussed in this research.  Furthermore, Raman spectroscopy has the advantage of being able to analyze processes *in situ*.  In this study *in*

*situ* Raman spectroscopy is performed by utilizing a high temperature heating stage and annealing the ND powder while simultaneously collecting Raman measurements at the elevated annealing temperatures.

### 4.    Ultraviolet Resonance-Enhanced Raman Spectroscopy

Although Equation (7) gives us insight on how to increase the intensity of the Raman signal, Raman spectroscopy, in general, still faces a few limitations.  First, the polarizability, or vibrational Raman cross-section, of materials is usually small which necessitates an increase in laser power or detector sensitivity.  Second, the signal to noise ratio is further reduced by inherent noise sources such as fluorescence.

Fluorescence is a form of luminescence, the emission of light by a material due to the absorption and conversion of energy into electromagnetic radiation [47]. Luminescence processes that occur over a nanosecond time scale or shorter are typically labeled as fluorescence.  Raman signals can be masked by the broad featureless spectra of fluorescence if the resonance Raman spectroscopy occurs via the same electronic excited states where fluorescence originates [45].  However, Raman and fluorescence signals are of different energies as fluorescence normally occurs from the lowest energy excited states.  Additionally, Raman scattering occurs on the femtosecond ($10^{-15}$ s) time scale directly from the high excited state while fluorescence occurs on the order of nanoseconds ($10^{-9}$ s).

Most Raman measurements are performed with lasers having wavelengths in the visible or near-infrared (IR) due to their commercial availability and cost.  However, visible and near-IR laser photon energies are below the first electronic transition of most molecules.  A UV laser has shorter wavelength and thus a higher photon energy, which lies within the electronic spectrum of the molecule, causes the intensity of the Raman-active vibrations to increase by orders of magnitude.  This effect has been given the label "resonance-enhanced" Raman scattering.  UV resonance-enhanced Raman spectroscopy takes advantage of this effect to produce stronger Raman signals and increased signal-to-

noise ratios (SNR). Figure 9 shows a schematic detailing the increased transitions to excited states in resonance-enhanced Raman scattering compared to standard Raman spectroscopy.

A UV excitation source was chosen in this Raman spectroscopy study of ND for multiple reasons. The Raman cross-section of diamond is small in the visible spectrum and graphite and amorphous carbon create a shielding effect around the diamond core [48]. ND Raman spectra collected from visible excitation sources can be dominated by features of non-diamond species and strong fluorescence may be produced which can mask the desired Raman spectra or require extensive background subtractions or baseline corrections [49].

Therefore, an excitation source with energy closer to the bandgap of diamond (5.5 eV) is necessary to utilize the resonance-enhancement and increase the Raman signal. To take advantage of the resonance effect yet still minimize undesired effects caused by higher energy lasers (such as sample heating), a 325 nm wavelength (3.82 eV) HeCd laser was utilized.
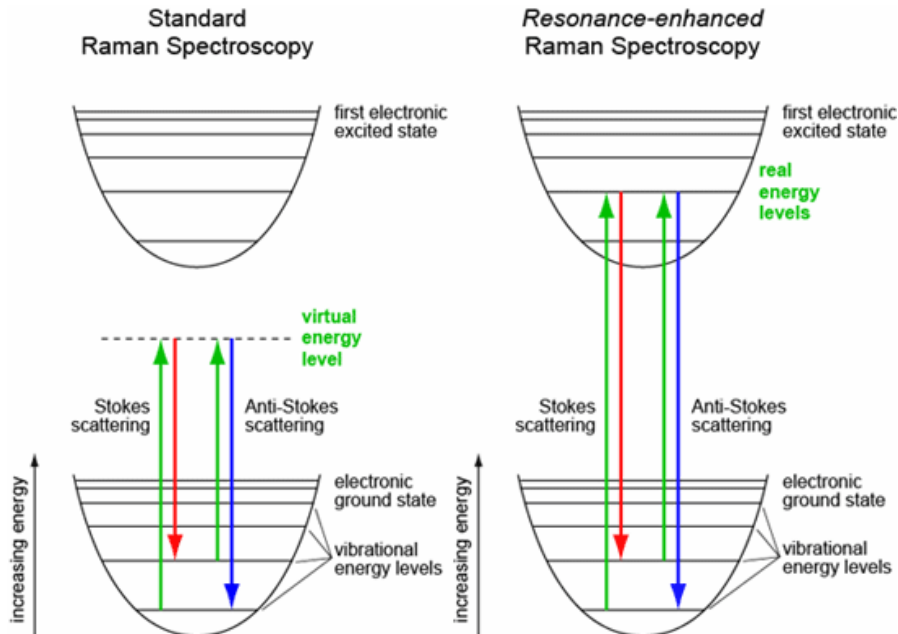


Figure 9.    Energy transitions which cause Raman Stokes and anti-Stokes scattering in standard Raman spectroscopy and resonance-enhanced Raman spectroscopy (From [50]).

## D.    THESIS OBJECTIVES

In this study, we employ *in situ* Raman spectroscopy to monitor the nanodiamond-to-carbon onion transformation during thermal annealing of ND powders. Specifically, this study aims to:

- Determine and evaluate the physical state of the ND at each annealed temperature.

- Determine the temperatures at which ND graphitization occurs and at which bulk carbon onion formation is observed.

- Determine the time dependence of these processes under isothermal conditions to obtain information on transformation kinetics and potential activation barriers.

- Utilize complementary characterization techniques (XRD, HRTEM, TGA) to support our Raman findings.

- Using the obtained data, determine the mechanisms by which these processes occur and compare the results with previous studies on ND annealing.

# II.   EXPERIMENTAL

## A.   MATERIALS

The detonation ND powder used for all experiments was purchased from International Technology Center (Raleigh, NC).   Diamond content and average ND crystal size, as determined by the manufacturer, are >98% and 4 nm, respectively.   The ND has a lattice parameter of 3.5550 +/- 0.0006 Å.   Figure 10 shows an HRTEM image provided by the manufacturer of the as-received ND powder.
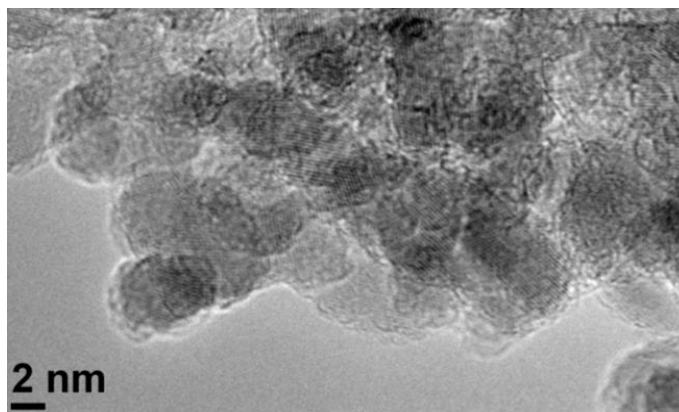


Figure 10.    HRTEM images of the as-received detonation nanodiamond powder (From [51]).

## B.   METHODS AND CHARACTERIZATION

### 1.   Raman Spectroscopy

Raman spectra were recorded using an inVia Confocal Raman Microspectrometer (Renishaw, UK) utilizing a 325-nm HeCd excitation laser, ThorLabs LMU-10X-NUV microscope objective, and a 3600 l/mm (lines per millimeter) UV diffraction grating.   To achieve an adequate SNR laser power was set to "100%" and "0%" focus (the laser was focused to the smallest area) within the Renishaw Wire software.   The spectrometer was calibrated using a single crystal industrial diamond assuming a position of the diamond optic mode peak at 1332 cm$^{-1}$.   Maximum laser power incident to all the ND samples was

measured to be ~275 µW as measured by a Newport 1928-C optical power meter. For the working distance used in all experiments, the laser beam spot diameter on sample was ~400 µm, yielding a laser spot area of area incident on sample was measured to be~ 0.13 mm$^2$, yielding a power density of ~2100 µW/mm$^2$. All *in situ* Raman experiments were conducted with a programmable water-cooled Linkam TS1500 high temperature stage. The ND powder sample was on a quartz slide within the stage. A constant Argon flow of ~40 ml/min at was provided during all measurements to prevent oxidation of the ND powder. Data analysis and curve fitting were performed using Renishaw's Wire 2.0 software. Figure 11 displays the experimental setup of the high-temperature stage in place below the UV microscope objective with Ar purge and cooling water connections.
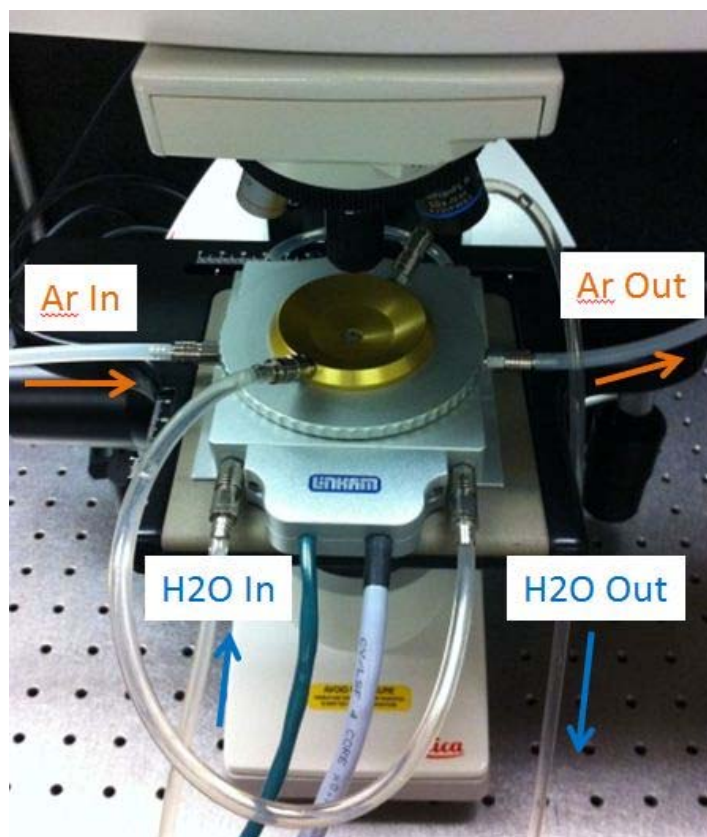


Figure 11.    Experimental setup for all Raman measurements of ND powder. Cooling water was used during all annealing experiments above room temperature. A constant Ar flow prevents oxidation of the ND powder.

### a.       *Laser Focusing Experiment 1*

The effect of the distance of the microscope objective to the sample (focal length) on the SNR and intensity of the obtained Raman spectra was investigated. Since the UV laser wavelength is not in the visible range, the UV light is not optimally focused when the sample is focused visually utilizing the microscope optics. The sample was focused visually then offset in the vertical direction utilizing software controlled and motorized Z stage before a Raman spectrum was collected. Collecting spectra for different focal lengths allowed the determination of the optimal UV focal length to be used for all subsequent experiments. Additionally, another separate experiment was performed in which the center frequency of the G band was measured while varying the UV laser focal length.

### b.       *Laser Exposure Experiment*

Many nanostructures, particularly ND, are prone to laser heating and laser-induced damage, even at low laser power [48, 52]. To investigate the quantitative effect of laser-induced thermal annealing of the ND, a ND sample was exposed to the UV laser without collecting Raman data, at 100% power and 0% focus, for 10 minutes at a time. In between each exposure interval, a Raman spectrum was collected at room temperature that lasted 3 minutes in duration. This experiment was repeated for three separate ND samples and the changes in the Raman spectra versus laser exposure time were analyzed. The location of incidence of the UV laser was not modified during each individual experiment.

### c.       *Annealing Experiment 1*

In the first series of *in situ* experiments, ND powder was heated from 25 to 900 °C in an inert atmosphere using the high temperature stage at rate of 10 °C/min. Raman spectra were recorded in increments of 100 °C.

### d.      *Annealing Experiment 2*

In the second part of the study, ND powder was heated from 25 to 1000 °C with a heat up rate of 10 °C /min.  At each 100 °C-temperature increment, the sample was annealed for 2 hours, and then cooled back to room temperature for Raman analysis. This procedure minimized the risk of laser heating-induced changes in the ND powders at elevated temperatures.

### e.      *Isothermal Annealing Experiments*

To explore the time dependence of the annealing process, ND samples were annealed isothermally at temperatures of 500, 600, 700, and 800 °C.  At different time increments ranging from 15 minutes to 8 hours depending on the annealing temperature, the sample was cooled to room temperature and Raman spectra were recorded.

### f.      *Laser Focusing Experiment 2*

In order to investigate slight differences of results conducted on different days with different samples, the effect of changes in the focal plane on G band peak position were tracked.  Similar to the laser focusing experiment 1, Raman spectra were collected at room temperature of the as-received ND powder.  Using the same area of the sample, first the sample area was brought into visual focus where multiple spectra were collected.  Without moving the sample area, the focal plane was moved between -400 to -1900 μm away from visual focus (the more negative, the shorter the distance between the objective and the sample).  Raman spectra were collected at different focal lengths and the G band peak position was plotted.

## 2.      Bulk Annealing and Characterization

Finally, to demonstrate the scalability of the annealing process and to verify the obtained results, bulk samples of ND powder were annealed in a tube furnace (MTI) under argon atmosphere for 12 hours at temperatures ranging from 500 °C to 1100 °C in 100 °C intervals, using a heating rate of 10 °C/min.  Approximately 0.30 grams of ND

was annealed at each temperature. Figure 12 shows a schematic and photograph of the experimental setup for the furnace annealing. In addition to Raman spectroscopy the following characterizations were performed on the bulk annealed powder.
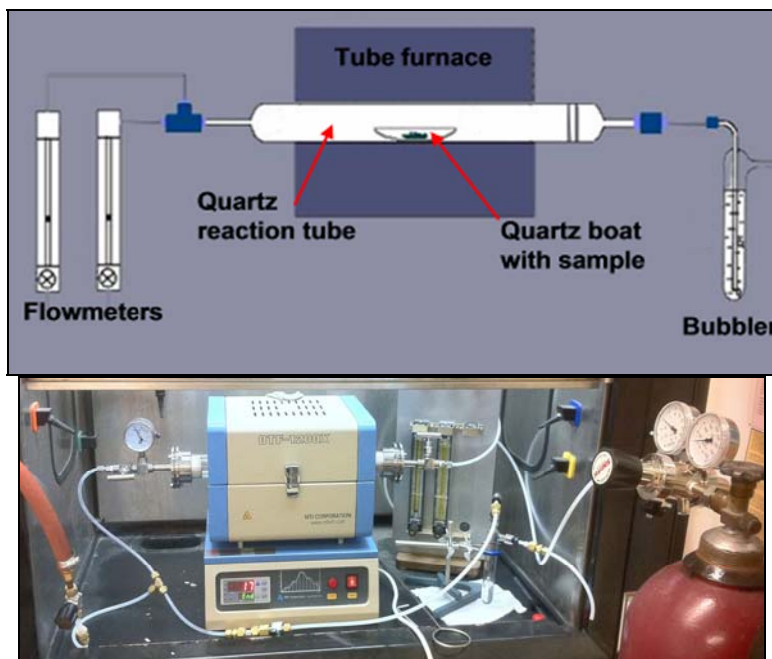


Figure 12.    Schematic drawing (top) and photograph (bottom) of the experimental setup used for tube furnace annealing of ND powder at 500–1100 °C.

### a.    *High Resolution Transmission Electron Microscopy*

High-resolution transmission electron microscopy (HRTEM) was performed using a Jeol JEM-2100 microscope (Jeol, Japan) at 100 keV. Carbon samples were dispersed in isopropanol and deposited on a lacey carbon grid. HRTEM images were collected at Drexel Nanotechnology Institute (Philadelphia, PA) while image selection and preparation was performed at NPS.

### b.    *X-ray Diffraction*

X-ray diffraction spectra were recorded with a Phillips PW 1830 diffractometer using a Cu source (x-ray wavelength ~0.154 nm) and an acceleration

voltage and anode current of 35kV and 30mA, respectively. XRD diffraction spectra were measured over the 2Θ range of 5 to 100° with a step size of 0.010°, 2.00 sec per step, yielding a 5 hour and 17 minute measurement time. Before analysis, the diffraction spectra were stripped of all K- α 2 wavelength radiation counts using the Rachinger method within the Xpert Highscore software.

### c. *Thermogravimetric Analysis*

Thermogravimetric analysis (TGA) was performed using a Q50 thermogravimetric analyzer (TA Instruments, USA). Samples of ~10 mg were studied between 25 °C and 1100 °C with a 2 hour isothermal period at 200 °C for outgassing using a 2 °C/min heating rate. All measurements were performed in flowing air atmosphere. All TGA experiments were conducted at Drexel Nanotechnology Institute (Philadelphia, PA) and data preparation and analysis were performed at NPS.

# III.    RESULTS AND DISCUSSION

## A.    RAMAN SPECTROSCOPY

### 1.    Laser Focusing Experiment 1

In order to determine the optimal focal length for the UV laser, Raman spectra of ND powder were measured at focal lengths ranging from +500 μm (longer focal length) to -2000 μm (shorter focal length) away from the optical white-light focus of the powder surface or a visible edge of the powder on the sample holder within the heating stage. Figure 13 displays the normalized Raman spectra of ND powder for different UV focal lengths.  The spectra in Figure 13 illustrate the large affect that the focal length has on the intensity of focused light delivered to the sample through the objective.  When the sample is out of the focal plane of the UV light, the delivered laser intensity is lower and therefore the Raman scattered light intensity is less, thus producing a weaker Raman signal as predicted by Equation (7).  Not having the optimal focusing distance between the objective and the sample can produce other undesirable side effects such as sample heating or background fluorescence.  In this study it was determined that a focal offset of -1000 μm from the visual focal plane produced the best SNR as well as the strongest signal of the Raman peak from diamond bonding (~1320 cm$^{-1}$) in the Raman spectra. This parameter was utilized in all further UV Raman spectroscopy experiments on the ND powder.
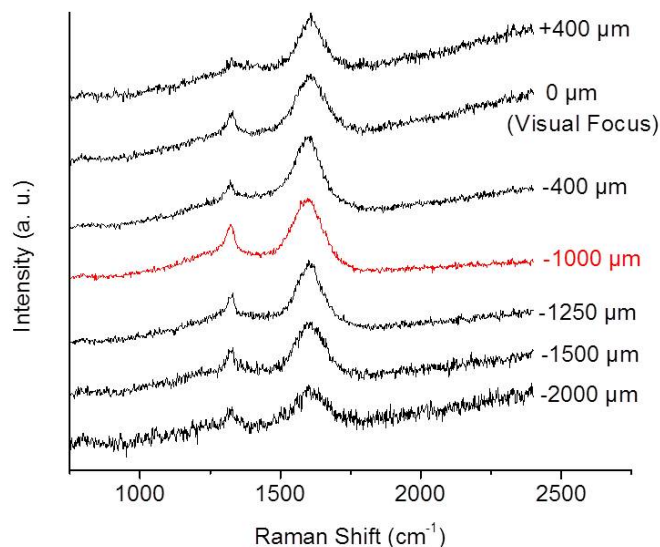
Figure 13.    Raman spectra of as-received ND powder with different focal lengths
between the microscope and the sample.

## 2.    Laser Exposure Experiment

Laser-induced heating of the sample is a known side effect of UV Raman spectroscopy due to the UV laser's increased energy per photon as compared to lasers in the visible or IR spectrum.  In this study, the primary goal is to determine the annealing temperature at which the ND starts to graphitize and transforms into a carbon onion. Therefore, additional sources of heating must be minimized, or at very least, quantified so that they can be taken into consideration when analyzing the results.

After performing baseline subtractions on each Raman spectra measured throughout the experiment, the intensity of the diamond peak ($\sim$1320 cm$^{-1}$) and G band peak ($\sim$1600 cm$^{-1}$) were determined by the curve fitting procedure as described in section III.3.  The ratio of the diamond-to-G band intensities is an important quantity in our annealing study that is further discussed below.  In short, this ratio decreases as a direct result of the decrease of the number of sp$^3$ bonds in the sample.  However, it is critical to reveal the effect the laser by itself has on this quantity.  The diamond-to-G band intensity ratio is plotted as function of total cumulative laser exposure time (time of exposure from

experiment and time from each Raman measurement) for three separate experiments in Figure 14. The plotted data illustrates that indeed laser-induced annealing occurs and creates a linear decreasing trend in the diamond to G band intensity ratio of the Raman spectrum of the ND powder. The colored solid lines are a linear fit for each data set. The average slope of the three linear trend lines was found to be -0.00159 min$^{-1}$. This indicates that one could expect an average decrease in the diamond-to-G band intensity ratios for a Raman spectrum of ND powder of 0.00159 per minute as a result of laser exposure alone. The results in Figure 14 were for a constant position of the laser on the ND sample. Using 0% laser focus, the laser beam only covers a very small area of the entire sample. As the Raman signal of ND is generally very weak, even under resonance condition (UV excitation), a balance between an acceptable SNR and laser-heating must be found. Therefore, it is concluded that the laser annealing affect can be minimized by keeping Raman measurement times low in conjunction with randomly scattering measurement points on the sample. Taking advantage of these two factors it was determined that for further UV Raman measurements of ND powder the effects of laser annealing were within the experimental error values of each measurement and need not be accounted for numerically. It was experimentally determined that a Raman measurement time of 6 minutes per spectra (18 accumulations and 20 seconds per accumulation) provided a good tradeoff between adequate SNR while still minimizing sample laser exposure. It is also important to note that the ND powder was in an inert atmosphere (continuous Argon purge) for these experiments. Subjected to 100% laser power the ND would instantaneously oxidize in air [53] and Raman analysis would lose its non-destructive character.
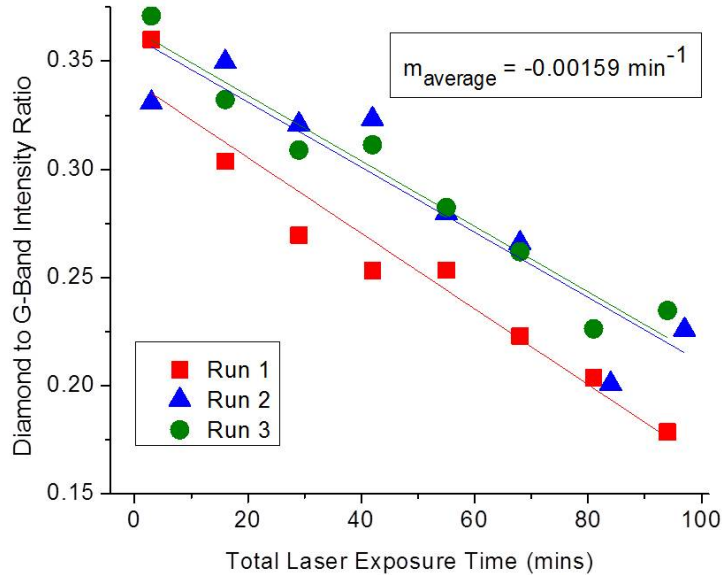
Figure 14.    Effect of laser exposure on ND powder.


## 3.      Annealing Experiment 1

Figure 15 shows the UV Raman spectrum of the as-received ND powder (at room temperature).  The spectrum contains two major Raman features: a down-shifted and asymmetrically broadened diamond peak at ~1320 cm$^{-1}$ and a broad band peak centered around ~1600 cm$^{-1}$, often simply referred to as "G-band" in analogy to sp$^2$-containing (graphitic) carbon materials.  However, as demonstrated in previous studies, this Raman band is typically a superposition of at least three separate peaks assigned to O-H bending vibrations (~1640 cm$^{-1}$) C=O stretching vibrations, (1740 cm$^{-1}$) and sp$^2$ carbon band (1590 cm$^{-1}$) [48].  The inset in Figure 15 displays the corresponding truncated and baseline-corrected spectrum used for peak fitting.  To simplify the fitting procedure and allow for unambiguous data interpretation, Raman spectra were fitted using only 3 constituent peaks.  Two peaks were required to account for the asymmetric line-shape of the diamond peak and one peak was used to represent the G band.  While the proposed fitting procedure is an oversimplification, it allows for a qualitative analysis and enables the monitoring structural changes during annealing.  At higher annealing temperatures

(>800 °C), accurate peak fitting was hindered by the simultaneous disappearance of the diamond peak (~1320 cm$^{-1}$) and the appearance of D band (~1380 cm$^{-1}$), requiring further modification of the fitting procedure. To properly analyze the Raman spectra, even at high annealing temperatures, a "simple" fitting method was introduced, in which the intensity and position of the G band and the diamond peak, as well as the intensity of the D-band at 1380 cm$^{-1}$ were measured directly from the Raman spectra, without computational peak fitting. The results of both the "normal" and "simple" fit were plotted for comparison at low temperatures to verify the suitability of the approach.
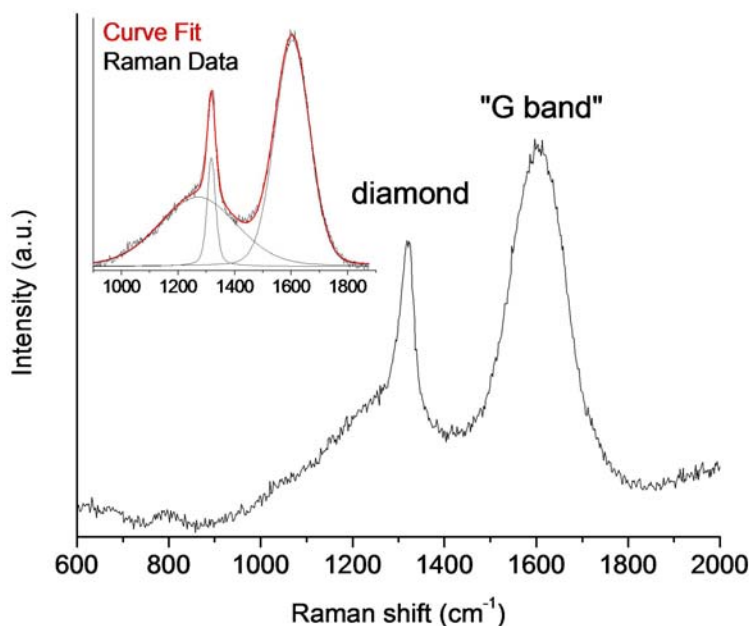


Figure 15.    Raman spectrum of as-received ND powder. The inset shows the truncated and baseline corrected spectrum and results from curve fitting (normal fit).

The *in situ* UV Raman spectra recorded during annealing of ND are shown in Figure 16. Several changes were observed during annealing. The G band becomes narrower and shifts to lower wavenumbers. The diamond peak shifts to lower wavenumbers and decreases in intensity relative to the G-band as the annealing temperature increases. At 900 °C, the diamond peak disappears while the disorder induced D band signal emerges at ~1400 cm$^{-1}$.

27
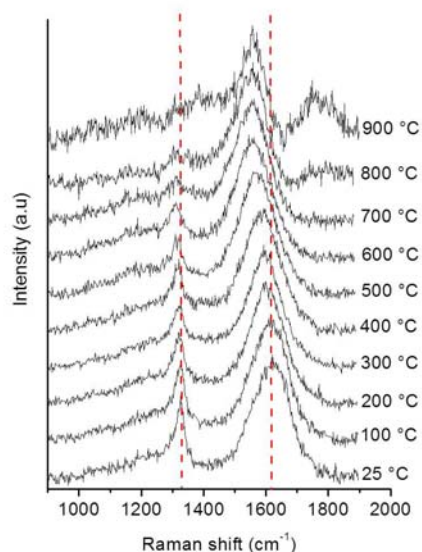
Figure 16.    *In situ* UV Raman spectra recorded during annealing of ND powder in Ar
atmosphere.  Spectra are normalized with respect to the maximum G band
intensity.  The vertical dotted lines are centered on the diamond and G band
peaks of the un-annealed as-received ND.

In order to obtain more quantitative information on the temperature-induced
changes during annealing, all Raman spectra were analyzed using the normal and
simplified fitting procedures.  Figure 17 illustrates the changes in peak position and peak
width (FWHM) of the G band and diamond peak Raman features.  As the annealing
temperature increases from 25 to 400°C, the G band shifts linearly towards lower
wavenumbers, as expected.  However, the temperature-induced downshift (~0.074 $cm^{-1}$/°C) is much larger than the values observed for the G band of most $sp^2$-carbon
containing nanomaterials, which typically ranges between 0.023 and 0.030 $cm^{-1}$/°C. [54-
56].  The observed discrepancies may be explained by the fact that the G-band of ND is
composed of three separate Raman features and contains contributions from surface
functionalities that exhibit different temperature behavior.  For example, removal of
moisture from the ND surface during annealing would reduce the Raman intensity at
higher frequencies (1620 $cm^{-1}$) and the resulting changes in the Raman spectra would
appear as a downshift of the G-band.  A second contribution may arise from laser-
induced sample heating, which can increase the temperature in the sample substantially,

in addition to the external heating provided by the stage [48, 52]. The temperature-induced shift of the G band increases between 400 and 600 °C, weakens upon further heating to 800 °C, and is reversed when reaching 900 °C, suggesting structural and/or compositional changes in the sample. The FWHM of the G band decreases between 25 to 300 °C, which can be attributed to the desorption of moisture and/or decomposition of oxygen-containing functional groups. Between 300 and 500 °C, the FWHM increases from ~130 to 147 cm$^{-1}$, followed by a steep decline to ~70 cm$^{-1}$ at 900 °C. The reduction in FWHM at high temperatures may be ascribed to the graphitization of the ND crystals, that is, the conversion of sp$^3$- to sp$^2$-bonded carbon. The slight increase in FWHM between 300 and 500 °C may indicate the formation of a highly amorphous sp$^2$-phase at lower temperatures, which becomes more graphitic as the temperatures increases. While temperatures in the range 300-500 °C seem too low for ND graphitization to occur, actual temperatures in the sample are likely higher due to additional, laser-induced heating. The temperature-induced downshift of the diamond peak was measured between 25 and 500 °C and found as ~0.020 cm$^{-1}$/°C. For both the G band and the diamond peak, the normal (squares in Figure 11) and the simple (triangles in Figure 11) fitting procedures yield similar results, suggesting that the proposed simplification of the fitting procedure is a suitable method for a qualitative analysis of the obtained Raman data.
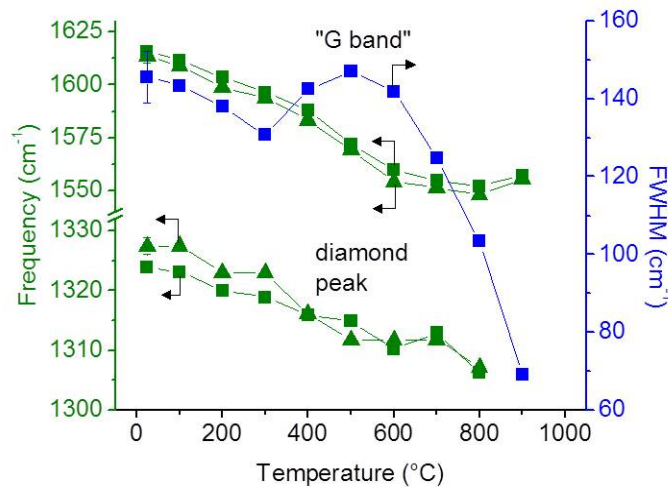


Figure 17.    Changes in Raman frequency and FWHM of the G Band and diamond peak during thermal annealing of ND. Squares and triangles represent data obtained from the normal and simplified curve fitting.

Figure 18 displays the temperature-dependence of several important intensity ratios that are typically used to evaluate the composition and structural ordering in carbon materials. The diamond-to-G band ratio (Dia/G) is used to determine the $sp^3/sp^2$ ratio, or diamond content [48, 57], whereas the D band-to-G band ratio (D/G) is commonly used to evaluate the structural ordering of the $sp^2$-phase (e.g., level of graphitization) [58]. Intensity and integrated intensity refer to the peak height and peak area, respectively. The integrated intensity takes into account contributions from species that exhibit different levels of ordering or different bonding configurations, whereas the intensity ratio reflect the contributions of the species with the most prominent Raman signal (maximum intensity). Both Dia/G intensity and integrated intensity ratios decrease with increasing annealing temperature. Again, results obtained from the normal and the simplified fitting procedures are in good agreement. While ND annealing is not expected at temperatures below 600 °C, these results demonstrate that laser-induced heating cause ND annealing at much lower temperatures and that laser-induced sample damage is an omnipresent risk during Raman analysis of ND powders, even in an inert atmosphere. The D/G ratio remains fairly constant over a wide temperature range, but increases rapidly above 800 °C, suggesting the onset of substantial graphitization around 900 °C. While there is no noticeable D band at lower annealing temperatures, the D/G ratio was determined using the simplified fitting method which is based on the absolute Raman intensity at 1380 cm$^{-1}$. Furthermore, the D band requires the presences of hexagonal rings and does not accurately represent the $sp^2$ carbon content. The increase in D/G at lower annealing temperatures may be caused by changes in the G band composition, such as removal of surface functional groups.
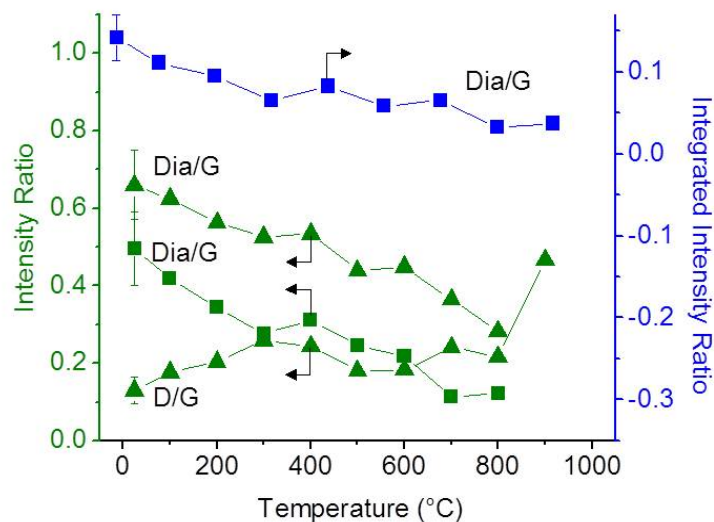
Figure 18.    Changes in diamond-to-G band (Dia/G) and D band-to G band (D/G) intensity and integrated intensity ratios.

The *in situ* experiment was subject to competing factors that contributed to the observed changes in the Raman spectra of ND during annealing.   Particularly, the simultaneous contributions from structural and compositional changes due to ND annealing, temperature-induced Raman shifts, fluorescence, and laser-induced changes in the sample, did not allow for a clear separation of the different effects and we were unable to isolate the individual contributions to the observed changes.   These effects increased and became unmanageable at higher temperatures mitigating the ability to obtain useful data therefore limited the experiment to a maximum temperature 900 °C.

## 4.        Annealing Experiment 2
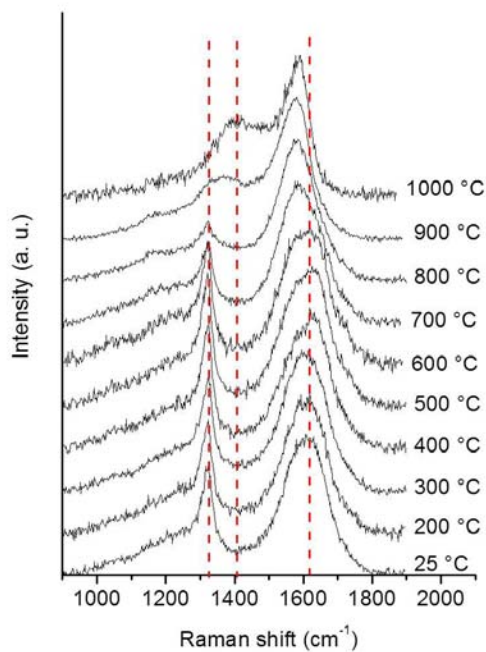


Figure 19.    Raman spectra of ND measured at room temperature after annealing for 2hrs at different temperatures between 25 and 1000 °C.  The vertical dotted lines are centered on the diamond and G band peaks of the un-annealed as-received ND as well as the center of the D band at the final annealing temperature of 1000 °C.
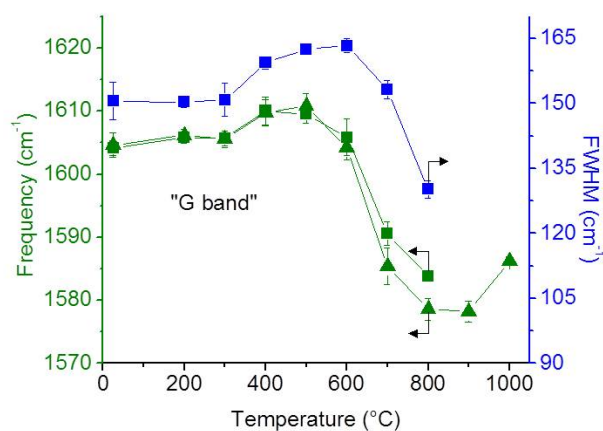


Figure 20.    Changes in Raman frequency and FWHM of the G Band.  Squares and triangles represent data obtained from normal and simplified curve fitting. Normal fit and simplified fit show similar trends.

32

In the laser exposure experiment it was concluded that at room temperature, structural changes in the ND powder due to laser-inducing heat resulting from UV laser exposure in the time required to collect a UV Raman spectra with adequate SNR was minimal. However, the previous experiment showed that the relative effects of the UV laser on the Raman spectrum are not constant and are amplified when the ND powder is at elevated temperatures. Therefore, in order to minimize the effect of laser-heating on the annealing process, a second series of experiments were conducted in which Raman spectra were recorded at room temperature after annealing ND for 2 hours at different temperatures in the range 200–1000 °C (Figure 19). As in Figure 16, the vertical dotted lines are centered on the diamond and G band peaks on the un-annealed as-received ND. In this case, any of the observed changes cannot be ascribed to temperature effects, but must be assigned to structural and/or compositional changes within the sample. Changes in the position and FWHM of the G band during annealing are shown Figure 20. At lower annealing temperatures (<300 °C) both position and FWHM of the G band remain fairly constant, suggesting that no structural and/or compositional changes occur at low temperatures. This observation supports our assumptions that laser heating led to the temperature-induced downshift of the G band observed even at low temperatures during *in situ* studies (Figure 17). Between 300 and ~500 °C, both position and FWHM of the G band increase, followed by a step decline in the temperature range ~500–800 °C. While the decrease in FWHM and the downshift of the G band starting around 500–600 °C likely characterize the onset of ND annealing, the interpretation of the increase of both values that precedes the annealing are not as straightforward. A more rigorous analysis of the G band of the 400 °C-annealed and 500 °C-annealed sample suggest that the relative change in intensity between the Raman contributions from C-C ($\sim$1590 cm$^{-1}$) and O-H (1620 cm$^{-1}$) species may cause the observed changes. However, further interpretation of these changes is difficult as they may result from a variety of structural and/or compositional changes. For example, structural changes, such as increased ordering (e.g., changes in bonding type, length and/or angle), are known to affect the Raman scattering cross section and thus the Raman intensity, while compositional changes, including removal or transformation of surface groups and localized sp$^3$-to-sp$^2$

conversions, also contributes to the observed discrepancy. However, since the increase in position and FWHM of the G band were also observed during the *in situ* experiments and is not within the experimental error range, it appears to be a real phenomenon that requires further investigation. Between 800 and 900 °C, the G band position remained fairly constant, and exhibits a slight upshift after annealing to 1000 °C. No noticeable shift of the diamond peak was observed after annealing as seen in Figure 21.
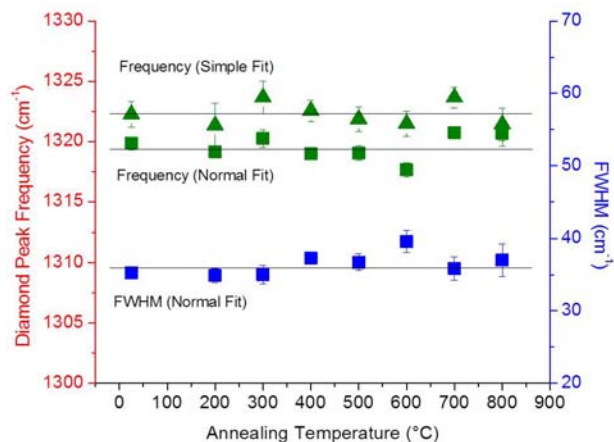


Figure 21.    Trend of Raman frequency and FWHM of the diamond peak. No significant shifts or changes were observed. No diamond peak was observed at annealing temperatures greater than 800 °C.

The intensity and integrated intensity ratios between the diamond peak and the G band show similar trends, indicating the onset of ND graphitization around 600 °C. The relative diamond peak intensity is constant until 300 °C, increases at 400 °C, and decreases approximately linearly to 800 °C. The reduction of the diamond peak intensity indicates that physically there is less diamond bonding present in the sample. Additional characterization techniques will be able to determine the structure of the transformed material. As Figure 19 shows, no diamond peak is present at annealing temperatures above 800 °C. At 900 °C a broad disorder-induced (D band) peak at ~1380 cm$^{-1}$ emerges. At 1000 °C the D band increases in relation to the G band and slightly shifts toward higher wavenumbers. Additional characterization techniques will assist in relating the observed changes in the ND UV Raman spectra to physical structural changes of the ND crystals.

It was desired to continue this experiment to higher annealing temperatures however, precise atmospheric monitoring equipment is required in order to monitor the exact composition of the stage atmosphere at temperatures greater than 1000 °C and prevent oxidation and loss of sample. After annealing at a temperature of 1100 °C for 2 hours, not enough sample remained in the stage to perform a useful Raman measurement. Sample loss was either due to the sample being entrained and carried away by the Ar gas purge or due to a very small amount of oxygen present in the stage, the sample oxidized into carbon gases ($CO$, $CO_2$). The latter hypothesis seems more likely. Future experiments at higher temperatures will require a trace oxygen analyzer to ensure no oxygen is present in the stage prior to increasing to higher annealing temperatures, thus preventing sample oxidation leading to sample loss. All Raman spectra measured in this research showed no observable signs of oxidation, which would produce different results compared to annealing in a complete inert atmosphere.
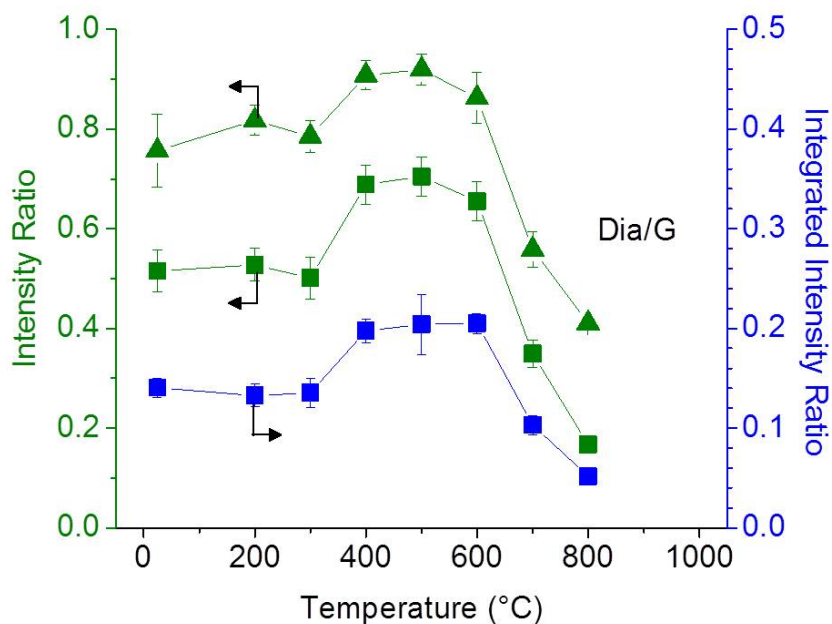


Figure 22.    Changes in diamond-to-G band (Dia/G) and D band-to-G band (D/G) intensity and integrated intensity ratios.

# 5.        Isothermal Annealing Experiments

In order to obtain further insight into the kinetics of the annealing process, the annealing of ND under isothermal conditions at 500, 600, 700, and 800 °C was monitored.  Raman spectra (Figures 23–25) were recorded at room temperature and the listed times represent the cumulative annealing time of each sample.  Raman spectra annealed at 500 °C showed very little change over 28 cumulative hours of annealing as illustrated in Figure 26 and are not shown.
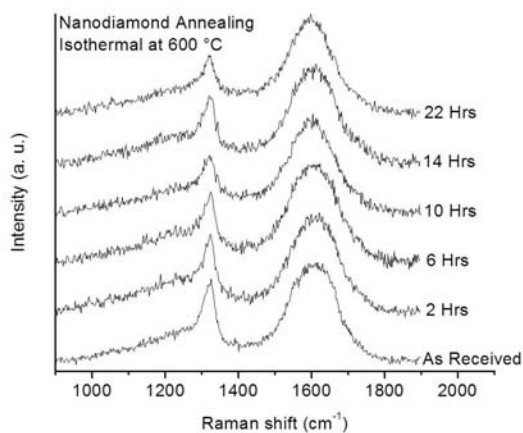


Figure 23.    Changes in Raman spectra of ND powder after annealing at 600 °C for 2, 6, 10, 14, and 22 hrs.
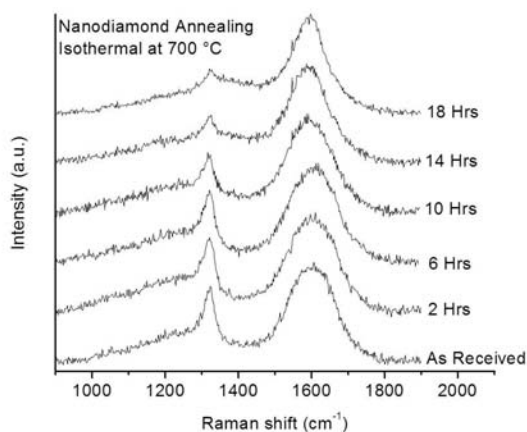


Figure 24.    Changes in Raman spectra of ND powder after annealing at 700 °C for 2, 6, 10, 14, and 18 hrs.
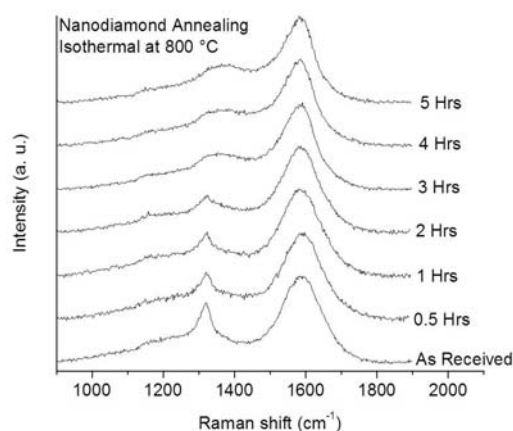
Figure 25. Changes in Raman spectra of ND powder after annealing at 800 °C for 0.5, 1, 2, 3, 4, and 5 hrs.

Annealing at 600 °C yielded slight changes in the Raman spectra over very long cumulative annealing times, 700 °C produced larger changes in less time, and 800 °C generated the fastest changes. Isothermal experiments were not conducted at 900 °C or higher as annealing experiment 2 showed that no diamond peak remained in the Raman spectrum after 2 hours of annealing at 900 °C. For example, Figure 26c shows that a diamond to G band intensity ratio of ~0.5 is reached at 500 °C in 20 hours, at 600 °C in 14 hours, and at 700 °C in 6 hours of accumulated annealing time. A diamond to G ratio of ~0.2 is reached at 700 °C in 14 hours yet only takes about 1 hour of annealing at 800 °C to reach the same value.

Figure 26a and 26b show the changes in G band position and FWHM after annealing at 500, 600, 700, and 800 °C, respectively. At low annealing temperatures (500 °C), a slight increase in both G band position and FWHM at the initial phase of the annealing process was observed, after which both values remained fairly constant. The increase in G band position and FWHM was also observed at 600 °C and 700 °C and has been discussed above. While it its origin cannot be identified with absolute certainty, it will recommended to be in the focus of future studies. Above 600 °C, both position and FWHM of the G band steadily decrease with annealing time due to the onset of ND graphitization, the conversion of $sp^3$-to-$sp^2$ carbon. The rate at which both G band

frequency and FWHM decrease increases with increasing annealing temperature and are highest at 800 °C. As discussed, similar trends were found for the diamond to G ratio, suggesting onset of ND transformation at temperatures around 600 °C (Figure 24c). This is further supported by the increase in the D/G ratio during the early stages of the $sp^3$-to-$sp^2$ conversion. The D/G ratio gives insights into the structural development of the $sp^2$ phase and is affected by both the ordering of the individual C-C bonds as well as the formation of the hexagonal rings that are the basis of the graphitic honeycomb lattice. While at 500 °C, the D/G ratio remains constant over the duration of the annealing experiment, it increases with time for annealing temperatures above 600 °C, whereas higher annealing temperatures lead to a more rapid graphitization rate and increased level of graphitization.
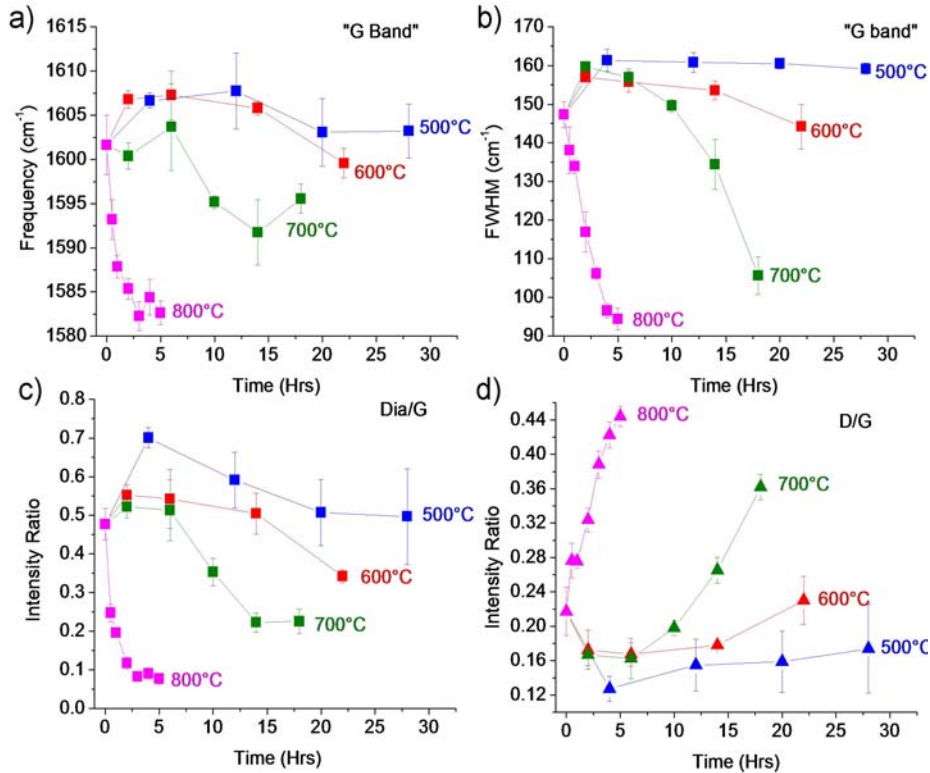


Figure 26.    Analysis of Raman spectra of ND powder after annealing at 500, 600, 700 and 800 °C for different annealing times between 2 and 28 hrs. Annealing under isothermal conditions led to a downshift of the G band (a) and reduction of the FWHM (b) for annealing temperatures above 600 °C. The Dia/G ratios (c) show similar temperature behavior, while the D/G ratio (d) increases upon ND annealing.

38

## 6.        Laser Focusing Experiment 2

Different samples of the same un-annealed as-received powder yielded slightly different measurements of the center of the G band peak for identical experimental conditions.  It was hypothesized that these small variations in results were due to small variations in the laser focal length due to the focusing process.  To test this prediction, Raman spectra were collected at room temperature at different focal lengths and the G band center frequency was determined for each spectrum utilizing both the normal and simplified spectra fitting methods as previously described.  Results plotted in Figure 27 demonstrate that small variations in the focal length can create measureable changes in the Raman shift of the G band.  These results appear to be linear for focal lengths 1900 to 900 μm smaller than the visual focal plane.  At longer focal lengths longer than -1000 μm (less negative numbers), the G band shifts toward lower wavenumbers then increases. While the precise reason for this is unknown, a possible reason could be that the focal plan of the UV laser lies within the sample, creating excessive sample heating, or the focal plane is located beneath the sample on the sapphire (aluminum oxide) sample holder which could produce adverse effects in the ND Raman spectrum.

This illustrates the importance in maintaining consistency of the focusing procedure prior to each spectrum.  Since the operator determines the visual focus by attempting to focus on the surface of the powder, or if not possible, a discernible edge or agglomeration of ND prior to using the motorized stage for the -1000 μm offset; a small amount of operator error can be introduced.  Therefore, to eliminate this effect and produce consistent results, care must be taken in sample preparation and focusing prior to each spectrum collection.
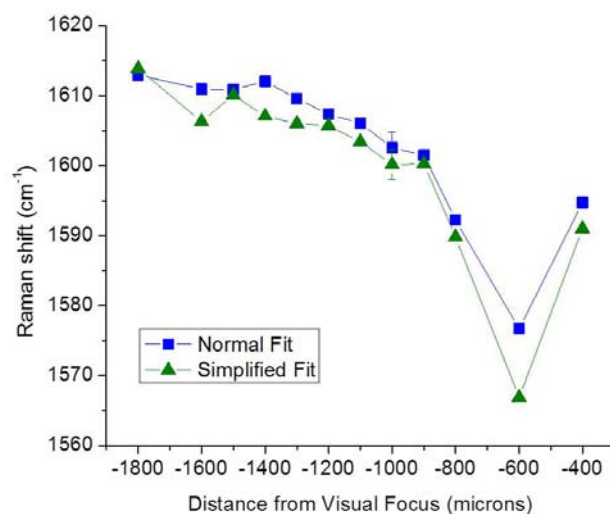
Figure 27.    G Band frequency measured with varying UV laser focal length

## B.    FURNACE ANNEALED SAMPLES

The results presented so far clearly indicate structural changes and onset of ND graphitization at or around 600 °C.  It is also evident that these changes occur more rapidly at higher annealing temperatures and that the diamond Raman signal disappears around 800–900 °C.  However, in order to obtain a comprehensive picture of the annealing process and allow for an unambiguous interpretation of the observed changes in the Raman spectra, more detailed information on ND structure and sample composition at the various stages of annealing is required.  Therefore bulk samples of ND were annealed in a tube furnace under various conditions for further characterization.  Figure 29a shows a photograph of a collection of seven ND powders annealed for 12 hours at different temperatures between 500 and 1100 °C.  The maximum design temperature limitations of the furnace restricted the maximum annealing temperature to 1100 °C.  The sample annealed at 500 °C does not show any noticeable color changes (silver grey) as compared to the as-received ND powder, in good agreement with Raman results.  After annealing at 600 °C, the ND appears slightly darker, turning the powder to a grey color.  Further increasing in annealing temperature to 700 and 800 °C yields a light brownish and a dark brownish grey, respectively.  At 900 °C, we noticed a significant

darkening to a brown black color, which further darkens after annealing at 1000 °C (dark brown black), and turns into black at 1100 °C. For verification and comparison, Raman spectra were measured on each furnace annealed sample. For consistency with all other experiments, the Raman spectra were measured with the sample in the heating stage including an identical steady Ar purge of ~40 ml/min. Raman spectra of the 12 hour furnace annealed samples are displayed in Figure 28 alongside the Raman spectra from the 2 hour heating stage annealing experiment (identical to Figure 19) for comparison. Although it was shown that at temperatures under 900 °C the transformation processes resulting from thermal annealing continue after 2 hours; the 12 hour annealed ND Raman spectra closely resemble those measured after only 2 hours of annealing. 12 hours of furnace annealing time was chosen precisely to verify this observation.
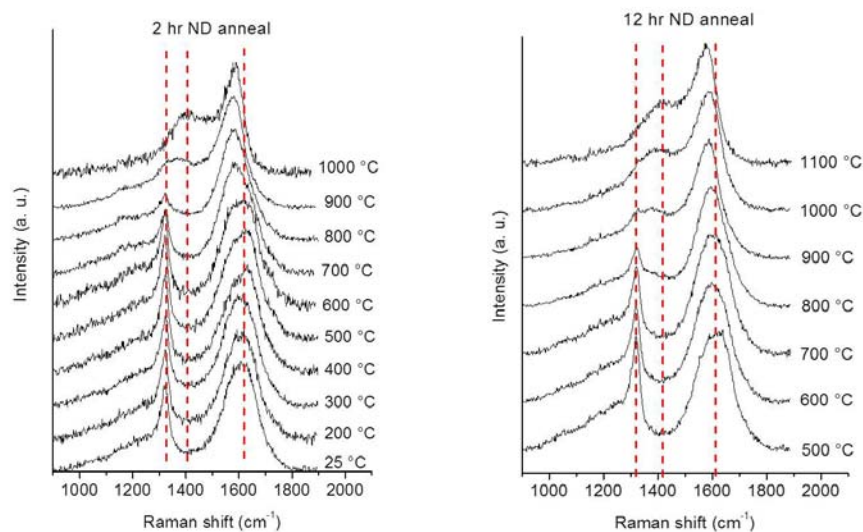


Figure 28.    Raman spectra of ND annealed in heating stage for 2 hours (left) alongside Raman spectra of ND annealed in tube furnace for 12 hours (right). The vertical dotted lines are centered on the diamond and G band peaks of the un-annealed as-received ND as well as the center of the D band at the final annealing temperature of 1000 °C.

The corresponding changes in the position and FWHM of the G band, and in the Dia/G and D/G ratios of the furnace-annealed ND samples are shown in Figure 26b and 26c, respectively. As expected, the intensity and integrated intensity Dia/G ratios

decrease with increasing annealing temperature until the diamond peak disappears around 900 °C. The D/G ratio (simple fit) remains fairly constant between 500 and 700 °C, but starts to increase at higher temperatures until reaching a maximum around 1000–1100 °C. The average measured frequency of the G band peak center was slightly lower than the anticipated trend comparing with the surrounding 500 and 700 °C data and the results from second high-temperature stage annealing experiment.  However, the standard deviation (error) of all the Raman spectra measured on the 600 °C furnace sample fell within the anticipated trend.  The larger-than-normal variations on these spectra could be caused by numerous variables including variations in UV focal plane and laser power. Overall, the observed color changes and corresponding trends in the Raman spectra are in good agreement with the results obtained from the annealing studies using the heating stage.
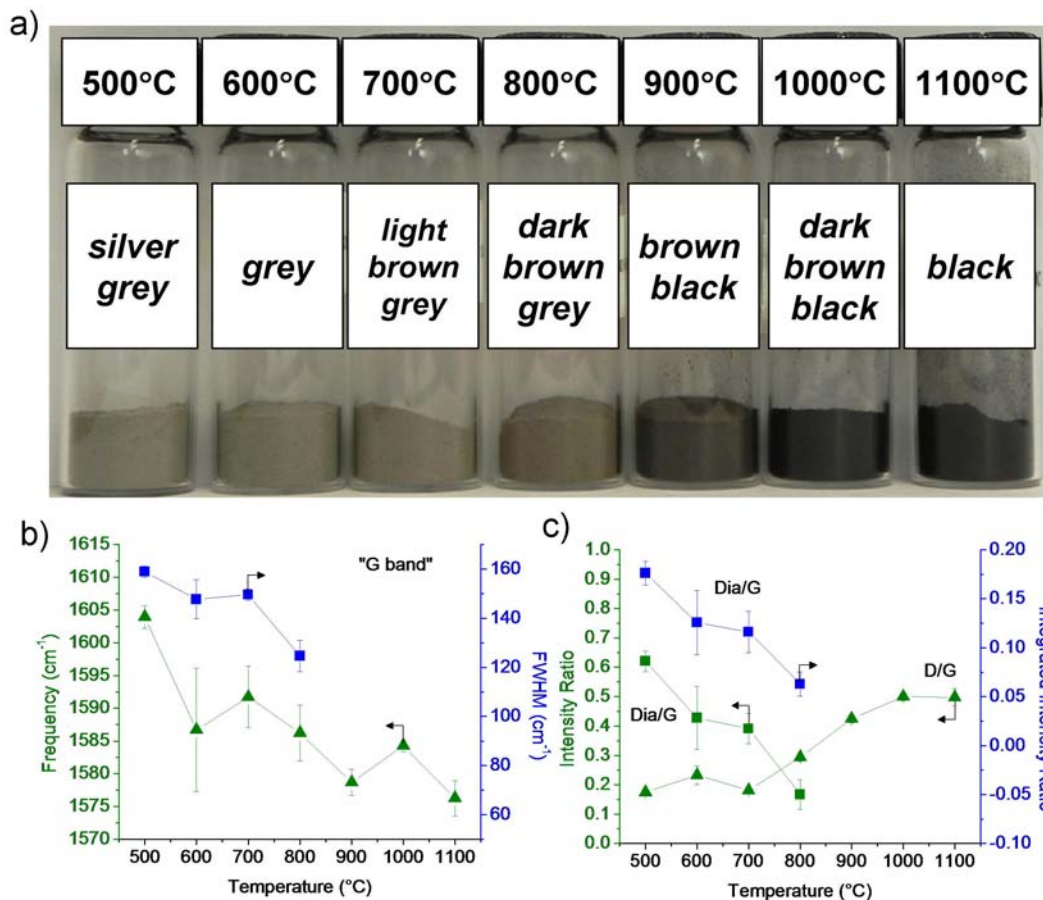
Figure 29.    a) Photograph of ND samples after annealing for 12 hrs at different
temperatures between 500 and 1100 °C under Ar atmosphere in a tube
furnace.  The corresponding changes in G band and various important
intensity ratios in the Raman spectra are shown in b) and c) respectively.

### 1.    High Resolution Transmission Electron Microscopy

While the reported changes in color and in Raman spectra are clear evidence for temperature-induced modifications of the bulk powder, several different annealing mechanisms may lead to the observed changes.  The first possible process is the preferential annealing of small-diameter ND crystals.  In this case, NDs below a critical diameter are partially or fully converted to carbon onions, while ND crystals above the critical parameter remain unchanged.

Figure 30.    HRTEM images of ND powders after annealing for 12 hours in a tube furnace at 700 °C (a), 800 °C (b), and 900 °C (c,d).  (HRTEM images taken at Drexel University, selection and image preparation conducted at NPS).

The second possible process involves the annealing of all ND crystals simultaneously, but at an annealing rate that is strongly size-dependent.  Depending on the temperature, the annealing mechanism may also change from the first to the second process.  In order to obtain further insights into the annealing mechanism we recorded several HRTEM micrographs from the annealed ND samples.  Figure 30 shows the HRTEM images of the ND powder after annealing for 12hrs at 700 (a), 800 (b), and 900 (c,d) in a tube furnace.  At lower annealing temperatures (≤700 °C) the ND powders do not exhibit any noticeable changes in crystal structure and size (image a).  The ND crystals are spherical in shape with sizes ranging from ~3 to ~30 nm.  The average ND crystal measures ~4–5 nm and shows a primarily diamond-structured surface.  After annealing at 800 °C (image b), the outer surface of the smaller diamond crystals (below ~15 nm) is converted to $sp^2$ carbon; however, the $sp^2$ carbon does not form a continuous,

closed shell, but is rather disordered in nature. At 900 °C, the transformation of the outer surface extends to larger diamond crystals (above ~15 nm), and some layered $sp^2$ carbon segments appear within the sample (Figure 29c and 29d), indicating a complete $sp^3$-to-$sp^2$ conversion of the smallest diamond crystals. However onion formation was not observed. Annealing at 1000 °C (Figure 31e) begins the process of producing layered $sp^2$ carbon, some of which forms layers of onion-like layers out of the smallest particles and on the exterior of larger particles. However, small and large ND crystals are still found throughout the sample. A further increase in annealing temperature to 1100 °C (Figure 31f,g,h) increases the structural ordering of the onions, making them fully concentric and spherical in shape. While the content of disordered $sp^2$ carbon is minimal, the sample still contains large ND crystals that are only partially converted (image g,h).

We have shown that UV Raman spectroscopy can detect the initial stages of the onset of ND graphitization however; HRTEM images reveal that a significant diamond structure is still present even though a diamond peak is not exhibited at annealing temperatures between 900 and 1100 °C. For this reason, further characterization of the ND is needed to obtain more structural information.
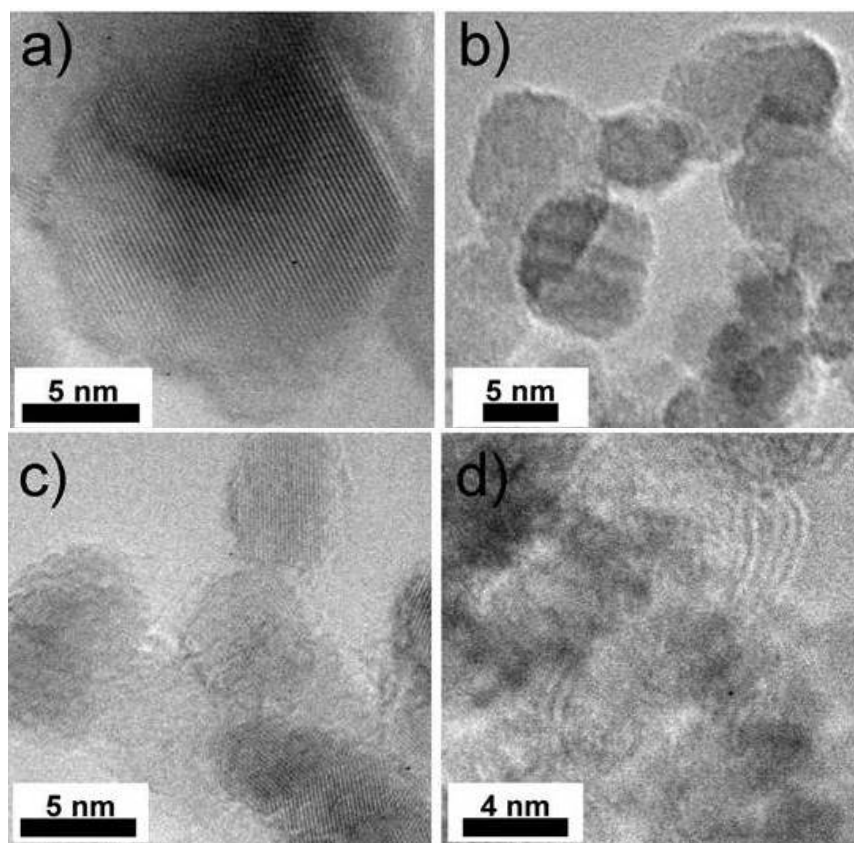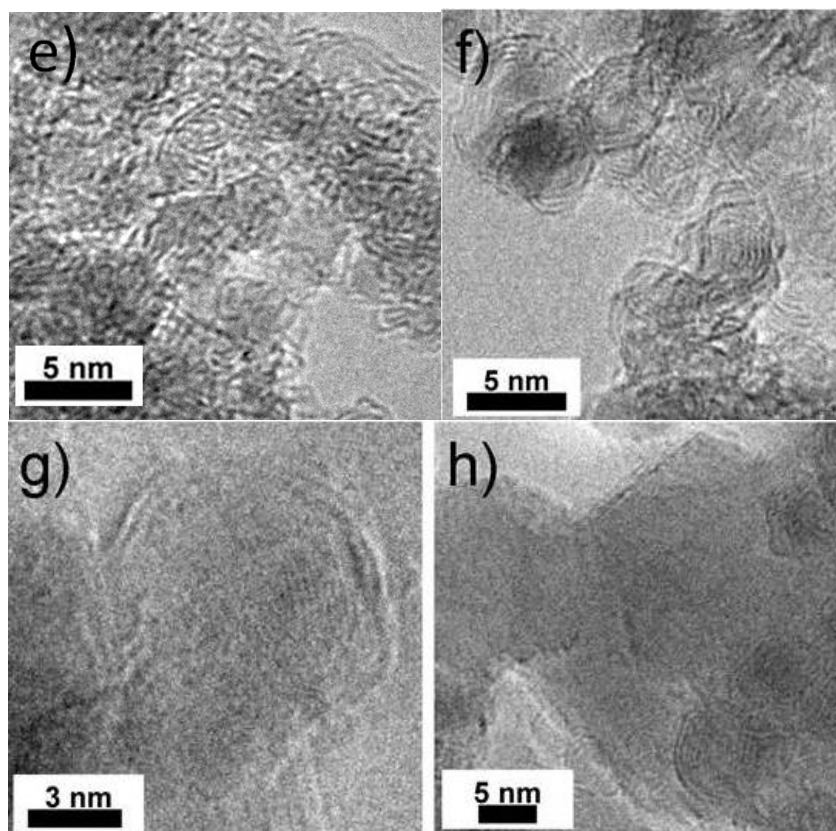
Figure 31.    HRTEM images of ND powders after annealing for 12 hours in a tube furnace at 1000 °C (e) and 1100 °C (f,g,h).  (HRTEM images taken at Drexel University, selection and image preparation conducted at NPS).

## 2.    X-ray Diffraction

Our results suggest that there is a strong dependence of the annealing rate on the ND crystal size.  Below 1000 °C small NDs are converted to carbon onions while larger NDs may experience only surface reconstruction.  When approaching 1100 °C, the majority of the ND crystal starts to transform to layered $sp^2$ carbon.  Larger ND crystals (>15 nm) appear only partially converted due to slower annealing kinetics.  These observations are supported by XRD data.  Figure 31a shows the low angle (2Θ) XRD patterns of the furnace-annealed powders.
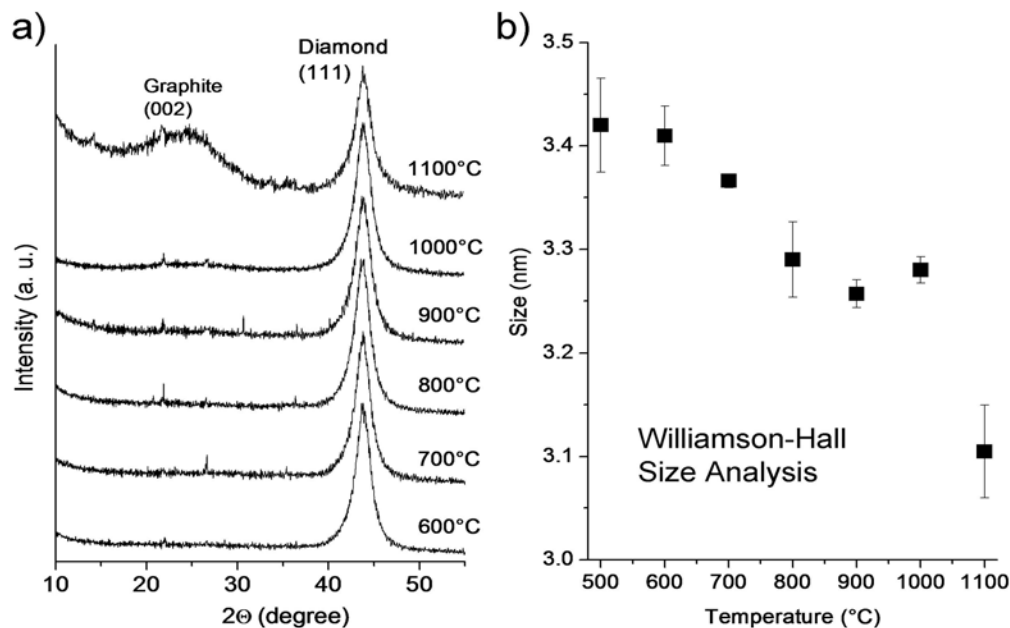
Figure 32.    a) X-ray diffraction pattern of ND powders after annealing for 12 hrs at different temperatures between 500 and 1100 C.

All samples exhibit a characteristic peak at ~43.7° which originates from the (111) planes of cubic diamond (sp$^3$), suggesting that ND is present in all samples, even at higher annealing temperatures.  Above 1000 °C, a second peak appears in the XRD pattern.  This feature results from the (002) planes of graphitic (sp$^2$) carbon.  While Raman spectroscopy is more sensitive to the sp$^2$ carbon forming on the crystal surface at the onset of ND annealing due to the larger Raman scattering cross section of sp$^2$ species, the detection of a XRD signal requires the simultaneous scattering from many crystal planes, and is therefore proportional to the crystal volume.  Surface effects are less noticeable and larger ND crystals contribute stronger to the overall XRD intensity.  Therefore, the XRD signal from surface sp$^2$ carbon formed at the onset of the transformation process is weak and is overshadowed by the more intense scattering of the diamond phase.  Even small ND crystals that have been fully converted to sp$^2$ carbon at lower temperatures (<900 °C) will be overshadowed by the strong signal of larger ND crystals that possess little or no sp$^2$ carbon.  Using XRD analysis, the annealing of the diamond phase may therefore not be monitored by the development of sp$^2$ phase, but by

47

probing the changes of the diamond core. Figure 32b shows the results of the Williamson-Hall (WH) analysis for the furnace-annealed ND samples. The data points in Figure 32b are averages of calculated particle size over a series of different curve fittings on the same XRD diffraction pattern. At this size scale, small changes in determining the FWHM and shape of the (111) diamond peak can have large effects on the calculated particle size. The error bars on Figure 32b represent the standard deviation of the calculations.

The WH analysis determines changes in diamond crystal size by evaluating the broadening of the diffractions peaks. Below 600 °C, no changes in ND crystal size were detected within the error range and the calculated values are similar to that of as-received ND (d = 3.4 nm). This is in good agreement with previous studies [42]. Between 700 and 900°C, the average crystal size decreases to 3.3 nm, and is further reduced to ~3.1 nm when reaching 1000-1100 °C. These results are in good agreement with HRTEM; however, it becomes clear that Raman spectroscopy and XRD must be considered complementary techniques when investigating the ND annealing process, as both characterization methods probe different parts of the sample. Raman spectroscopy is most sensitive to the onset of $sp^2$ carbon formation at the crystal surface, whereas XRD probes the diamond core and favors larger ND crystals. The results obtained from Raman spectroscopy studies revealed onset of ND annealing at temperatures as low as 600-700 °C, beginning with surface reconstruction of small ND crystals. However, no diamond Raman signal was detected above 900 °C. In contrast, XRD demonstrated presence of diamond at temperatures as high as 1100 °C, but noticeable contributions from $sp^2$ carbon were not observed below 1000 °C.

## 3.      Thermogravimetric Analysis
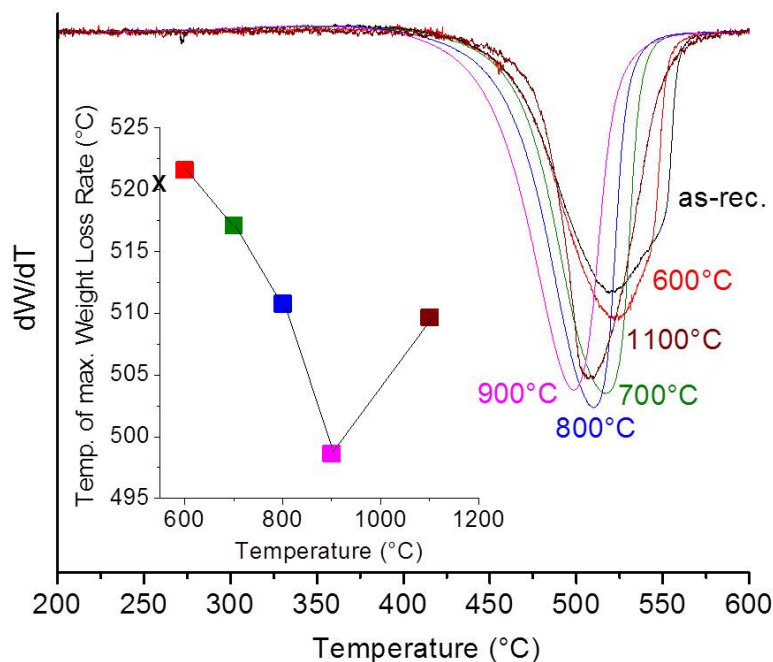


Figure 33.     TGA weight loss rate of furnace-annealed ND samples upon oxidation in air. The inset shows the temperature of the maximum weight loss rate as a function of annealing temperature. (TGA data collected at Drexel University, analysis and plotted conducted at NPS).

Finally, we investigated the thermal stability and the oxidation behavior of the various samples to further support the proposed annealing model.  Figure 33 shows the weight loss rate (differentiated weight loss curve) of the annealed samples recorded during TGA analysis in laboratory air, in comparison to as-received ND.  The inset displays the temperature of the maximum weight loss rate as a function of annealing temperature.  The black "x" on the y-axis indicated the value measured for as-received ND powder.  For the as-received and the 600 °C-annealed ND, the maximum weight loss occurs at around 520 °C and both samples exhibit a broad weight loss peak due to the wide size distribution and the known size-dependence of the oxidation resistance of ND crystals [59].  With increasing annealing temperature from 600 to 800 °C, the weight loss

peak becomes narrower and is downshifted to 517 and 511 °C at 700 and 800 °C, respectively.  The 900 °C-sample exhibits the lowest oxidation resistance (maximum weight loss at ~498 °C).  While below 900 °C, carbon onion formation was not observed, the conversion of the ND surface to amorphous $sp^2$ carbon lowers the activation energy for ND oxidation, even for larger ND crystals.  A further increase in annealing temperature reverses this trend.  At 1100 °C, the maximum weight loss occurs at 510 °C. This can be explained by the increasing structural ordering of the $sp^2$ phase and formation of carbon onions at higher annealing temperatures.

# IV. CONCLUSION

In studying the ND-to-carbon onion transformation during thermal annealing there are numerous factors that influence the identification of the graphitization mechanism and the conditions at which the $sp^3$-to-$sp^2$ conversion occurs including, but not limited to, ND crystal size and composition, annealing parameters, and characterization techniques. In this research, we have employed *in situ* UV Raman spectroscopy experiments to monitor the ND-to-carbon onion transformation as well as its time dependence.

Raman spectroscopy has proven to be a powerful tool for the characterization of ND powders as it allows for a fast and nondestructive evaluation of ND purity and surface state. X-ray diffraction (XRD), high resolution transmission electron microscopy (HRTEM), and thermogravimetric analysis (TGA) were also used to determine structural characteristics of the samples at various stages in the annealing process. Together, Raman spectroscopy, X-ray diffraction, HRTEM, and thermal analysis provide a comprehensive picture of the ND annealing mechanism. Based on this study, the following process steps are believed to take place during annealing:

- Annealing of ND powders starts with the $sp^3$-to-$sp^2$ conversion of the surface smaller ND crystals at temperatures as low as 600–700 °C.

- At 900 °C, the surface of the majority of the ND crystals is subject to $sp^3$-to-$sp^2$ conversion. Some of the smallest ND crystals are completely converted to $sp^2$-carbon and appear as layered structures; however, carbon onion formation is not observed.

- At 1000 °C, the majority of the ND crystals are converted to $sp^2$-carbon, but the rate of annealing is strongly dependent on the crystal size and highest for small ND crystals.

The findings reported in this work in close agreement with previous studies; however, our results provide deeper insight into the annealing mechanism, particularly the temperatures at which the surface of ND particles begin to transform to different phases of carbon and the manner in which this process proceeds as annealing temperature increases. However, similar research at increasing annealing temperatures must be

continued in order to gain a complete picture of the entire transformation process from as-received ND powder to completely annealed pure carbon onions and reveal the useful physical and electrochemical properties carbon onions and carbon onion-ND hybrid particles may possess.

# LIST OF REFERENCES

[1]     Ugarte, D., *Curling and closure of graphic networks under electron-beam irradiation* Nature, 1992. **359**(6397): p. 707–709.

[2]     Hirata, A., M. Igarashi, and T. Kaito, *Study on solid lubricant properties of carbon onions produced by heat treatment of diamond clusters or particles.* Tribology International, 2004. **37**(11-12): p. 899–905.

[3]     Shenderova, O., et al., *Detonation nanodiamond and onion-like carbon: applications in composites.* Physica Status Solidi a-Applications and Materials Science, 2008. **205**(9): p. 2245–2251.

[4]     Shenderova, O., et al., *Onion-like carbon for terahertz electromagnetic shielding.* Diamond and Related Materials, 2008. **17**(4-5): p. 462–466.

[5]     Hebard, A.F., et al., *Superconductivity at 18 K in potassium-doped C60.* Nature, 1991. **350**(6319): p. 600–601.

[6]     Sano, N., et al., *Properties of carbon onions produced by an arc discharge in water.* Journal of Applied Physics, 2002. **92**(5): p. 2783–2788.

[7]     Xu, B.S., et al., *A novel catalyst support for DMFC: Onion-like fullerenes.* Journal of Power Sources, 2006. **162**(1): p. 160–164.

[8]     Keller, N., et al., *The catalytic use of onion-like carbon materials for styrene synthesis by oxidative dehydrogenation of ethylbenzene.* Angewandte Chemie-International Edition, 2002. **41**(11): p. 1885–+.

[9]     Yang, Y., et al., *Ferromagnetic Property and Synthesis of Onion-Like Fullerenes by Chemical Vapor Deposition Using Fe and Co Catalysts Supported on NaCl.* Journal of Nanomaterials, 2011.

[10]    Han, F.D., B. Yao, and Y.J. Bai, *Preparation of Carbon Nano-Onions and Their Application as Anode Materials for Rechargeable Lithium-Ion Batteries.* Journal of Physical Chemistry C, 2011. **115**(18): p. 8923–8927.

[11]    Wang, H.Y., et al., *Graphitized carbon nanobeads with an onion texture as a lithium-ion battery negative electrode for high-rate use.* Advanced Materials, 2005. **17**(23): p. 2857–+.

[12]    Pech, D., et al., *Ultrahigh-power micrometre-sized supercapacitors based on onion-like carbon.* Nature Nanotechnology, 2010. **5**(9): p. 651–654.

[13]    Mostofizadeh, A., et al., *Synthesis, Properties, and Applications of Low-Dimensional Carbon-Related Nanomaterials.* Journal of Nanomaterials, 2011.

[14]    Elliott, B.C., *Synthesis, Electronic Structure, and Reactivity of Endohedral Metallofullerenes and Other Endohedral Carbons Nanostrucutes* in *Chemistry*2008, Clemson University: Clemson.

[15] Ugarte, D., *Morphology and structure of graphitic soot particles generated in arc-discharge C60 production* Chemical Physics Letters, 1992. **198**(6): p. 596–602.

[16] Xu, B.S. and S.I. Tanaka, *Formation of giant onion-like fullerenes under Al nanoparticles by electron irradiation.* Acta Materialia, 1998. **46**(15): p. 5249–5257.

[17] Nasibulin, A.G., et al., *Carbon nanotubes and onions from carbon monoxide using Ni(acac)(2) and Cu(acac)(2) as catalyst precursors.* Carbon, 2003. **41**(14): p. 2711–2724.

[18] He, C.N., et al., *Carbon onion growth enhanced by nitrogen incorporation.* Scripta Materialia, 2006. **54**(10): p. 1739–1743.

[19] Yang, Y., et al., *Synthesis of nano onion-like fullerenes by chemical vapor deposition using an iron catalyst supported on sodium chloride.* Journal of Nanoparticle Research. **13**(5): p. 1979–1986.

[20] Qiu, J.S., et al., *Formation of carbon nanotubes and encapsulated nanoparticles from coals with moderate ash contents.* Carbon, 1998. **36**(4): p. 465–467.

[21] Cabioc'h, T., et al., *Influence of the implantation parameters on the microstructure of carbon onions produced by carbon ion implantation.* Applied Physics Letters, 1998. **73**(21): p. 3096–3098.

[22] Bystrzejewski, M., et al., *Catalyst-free synthesis of onion-like carbon nanoparticles.* New Carbon Materials, 2010. **25**(1).

[23] Zhao, M., et al., *Large-scale synthesis of onion-like carbon nanoparticles by carbonization of phenolic resin.* Acta Materialia, 2007. **55**(18): p. 6144–6150.

[24] Kuznetsov, V.L., et al., *Onion-like carbon from ultra-disperse diamond* Chemical Physics Letters, 1994. **222**(4): p. 343–348.

[25] Bulusheva, L.G., et al., *Soft X-ray spectroscopy and quantum chemistry characterization of defects in onion-like carbon produced by nanodiamond annealing.* Diamond and Related Materials. **16**(4-7): p. 1222–1226.

[26] Deheer, W.A. and D. Ugarte, *CARBON ONIONS PRODUCED BY HEAT-TREATMENT OF CARBON SOOT AND THEIR RELATION TO THE 217.5 NM INTERSTELLAR ABSORPTION FEATURE.* Chemical Physics Letters, 1993. **207**(4-6): p. 480–486.

[27] Obraztsova, E.D., et al., *Raman identification of onion-like carbon.* Carbon, 1998. **36**(5-6): p. 821–826.

[28] Chen, J., et al., *Graphitization of nanodiamond powder annealed in argon ambient.* Applied Physics Letters, 1999. **74**(24): p. 3651–3653.

[29] Qiao, Z.J., et al., *Graphitization and microstructure transformation of nanodiamond to onion-like carbon.* Scripta Materialia, 2006. **54**(2): p. 225–229.

54

[30]    Leyssale, J.M. and G.L. Vignoles, *Molecular dynamics evidences of the full graphitization of a nanodiamond annealed at 1500 K.* Chemical Physics Letters, 2008. **454**(4-6): p. 299–304.

[31]    Kwon, S.J. and J.G. Park, *Theoretical analysis of the graphitization of a nanodiamond.* Journal of Physics-Condensed Matter, 2007. **19**(38).

[32]    Butenko, Y.V., et al., *The thermal stability of nanodiamond surface groups and onset of nanodiamond graphitization.* Fullerenes Nanotubes and Carbon Nanostructures, 2006. **14**(2-3): p. 557–564.

[33]    Bulusheva, L., et al., *Topology and electronic structure of onion-like carbon and graphite/diamond nanocomposites*, in *Nanophase and Nanocomposite Materials Iv*, S.P.J.C.V.R.A.L.G.Q.M.J.I. Komarneni, Editor 2002. p. 381–386.

[34]    Osipov, V.Y., et al., *Magnetic and high resolution TEM studies of nanographite derived from nanodiamond.* Carbon, 2006. **44**(7): p. 1225–1234.

[35]    Zou, Q., et al., *Fabrication of onion-like carbon using nanodiamond by annealing at lower temperature and vacuum.* Journal of Wuhan University of Technology-Materials Science Edition, 2009. **24**(6): p. 935–939.

[36]    Zou, Q., et al., *HRTEM and Raman characterisation of the onion-like carbon synthesised by annealing detonation nanodiamond at lower temperature and vacuum.* Journal of Experimental Nanoscience, 2010. **5**(6): p. 473–487.

[37]    Zou, Q., et al., *Transformation of onion-like carbon from nanodiamond by annealing.* Inorganic Materials, 2010. **46**(2): p. 127–131.

[38]    Zou, Q., et al., *Characterisation of onion-like carbon fabricated by annealing nanodiamond.* Materials Research Innovations, 2010. **14**(4): p. 285–288.

[39]    Zou, Q., M.Z. Wang, and Y.G. Li, *Onion-like carbon synthesis by annealing nanodiamond at lower temperature and vacuum.* Journal of Experimental Nanoscience, 2010. **5**(5): p. 375–382.

[40]    Xie, F.Y., et al., *Surface characterization on graphitization of nanodiamond powder annealed in nitrogen ambient.* Surface and Interface Analysis, 2010. **42**(9): p. 1514–1518.

[41]    Petit, T., et al., *Early stages of surface graphitization on nanodiamond probed by x-ray photoelectron spectroscopy.* Physical Review B, 2011. **84**(23).

[42]    Mykhaylyk, O.O., et al., *Transformation of nanodiamond into carbon onions: A comparative study by high-resolution transmission electron microscopy, electron energy-loss spectroscopy, x-ray diffraction, small-angle x-ray scattering, and ultraviolet Raman spectroscopy.* Journal of Applied Physics, 2005. **97**(7).

[43]    C.V. Raman, K.S.K., *A new class of spectra due to secondary radiation.* Indian Journal of Physics, 1928. **2**: p. 399–419.

[44]     *The Nobel Prize in Physics 1930.* [cited 2012 12 May]; Available from: http://www.nobelprize.org/nobel_prizes/physics/laureates/1930/.

[45]     Dieing, T., Hollricher, O., Toporski, J., *Confocal Raman microscopy* 2010, Berlin, Heidelberg: Springer-Verlag Berlin Heidelberg.

[46]     Larkin, P., *Infrared and Raman Spectroscopy; Principles and Spectral Interpretation*2011, London: Elsevier.

[47]     Kasap, S., *Principles of Electronic Materials and Devices*2005: McGraw Hill Higher Education.

[48]     Mochalin, V., S. Osswald, and Y. Gogotsi, *Contribution of Functional Groups to the Raman Spectrum of Nanodiamond Powders.* Chemistry of Materials, 2009. **21**(2): p. 273–279.

[49]     Osswald, S., et al., *Phonon confinement effects in the Raman spectrum of nanodiamond.* Physical Review B, 2009. **80**(7).

[50]     *UV Raman Spectroscopy.* [cited 2012 May 10]; Available from: http://www.semrock.com/uv-raman-spectroscopy.aspx.

[51]     *HRTEM Images of Polydispersed 'Standard' Nanodiamond.* [cited 2012 May 22]; HRTEM Images of Polydispersed 'Standard' Nanodiamond]. Available from: http://www.itc-inc.org/hrtem.html.

[52]     Osswald, S., K. Behler, and Y. Gogotsi, *Laser-induced light emission from carbon nanoparticles.* Journal of Applied Physics, 2008. **104**(7).

[53]     Osswald, S., et al., *Control of sp(2)/sp(3) carbon ratio and surface chemistry of nanodiamond powders by selective oxidation in air.* Journal of the American Chemical Society, 2006. **128**(35): p. 11635–11642.

[54]     Osswald, S., M. Havel, and Y. Gogotsi, *Monitoring oxidation of multiwalled carbon nanotubes by Raman spectroscopy.* Journal of Raman Spectroscopy, 2007. **38**(6): p. 728–736.

[55]     Osswald, S., E. Flahaut, and Y. Gogotsi, *In situ Raman spectroscopy study of oxidation of double- and single-wall carbon nanotubes.* Chemistry of Materials, 2006. **18**(6): p. 1525–1533.

[56]     Osswald, S., et al., *Elimination of D-band in Raman spectra of double-wall carbon nanotubes by oxidation.* Chemical Physics Letters, 2005. **402**(4-6): p. 422–427.

[57]     Osswald, S. and Y. Gogotsi, *In Situ Raman Spectroscopy of Oxidation of Carbon Nanomaterials*

[58]     *Raman Spectroscopy for Nanomaterials Characterization*, C.S.S.R. Kumar, Editor 2012, Springer Berlin Heidelberg. p. 291–351.

[59]     Ferrari, A.C. and J. Robertson, *Raman spectroscopy of amorphous, nanostructured, diamond-like carbon, and nanodiamond.* Philosophical Transactions of the Royal Society a-Mathematical Physical and Engineering Sciences, 2004. **362**(1824): p. 2477–2512.

[60]     Osswald, S., et al., *Increase of nanodiamond crystal size by selective oxidation.* Diamond and Related Materials, 2008. **17**(7-10): p. 1122–1126.

THIS PAGE INTENTIONALLY LEFT BLANK

# INITIAL DISTRIBUTION LIST

1.      Defense Technical Information Center
    Ft. Belvoir, Virginia

2.      Dudley Knox Library
    Naval Postgraduate School
    Monterey, California

3.      Sebastian Osswald
    Naval Postgraduate School
    Monterey, California

4.      Joseph Hooper
    Naval Postgraduate School
    Monterey, California

5.      Jonathan E. Cebik
    Naval Postgraduate School
    Monterey, California

6.      Andres Larraza
    Naval Postgraduate School
    Monterey, California